Statistical representative elementary area of shale inferred by micromechanics

Philippe Cosenza, Anne-Laure Fauchille, Dimitri Prêt, Stephen Hedan, Albert Giraud

Statistical Representative Elementary Area of Shale Inferred by Micromechanics

Intended for publication in International Journal of Engineering Science

Abstract

This paper provides new estimates for the Representative Elementary Area (REA) sizes of the following two shales that are actively being studied in the framework of deep disposal of radioactive waste: Callovo-Oxfordian (COx) claystone from the Meuse/Haute-Marne underground research laboratory (Eastern France) and Toarcian argillite from the experimental station of Tournemire (Southern France). The REA sizes, named L_{REA}, were obtained from two mineral maps following the classic "counting box" (CB) method and a statistical approach that introduces the concept of a "statistical" REA. Following this approach, a "statistical" REA is related not only to the microstructure and the properties of each of the components but, above all, to a given precision in the estimation of the effective property depending on the number of realizations that one is ready to generate. The probabilistic concept of realization is here, from a practical viewpoint, a subdomain of a mineral map in which the apparent morphological or mechanical properties have to be calculated. In this study, the apparent elastic moduli of the subdomain have been estimated using two micromechanical models. The first micromechanical model consisted of an inclusion-based model for which spherical nonclay grain is embedded in a clay matrix in which the values of its transverse isotropic stiffness tensor have been taken from literature. The second micromechanical model was an isotropic inclusion-based model for which a spherical nonclay grain is embedded in a clay matrix; the elastic moduli values have been inverted by a Monte-Carlo approach from the engineering moduli of both shales under study. Our calculations have shown the following results: (i) the statistical morphological L_{REA} considering the surface clay fraction are of the same order of magnitude as those measured in other shales and those obtained by the simple CB method, with relative error values between 5 and 10%, (ii) the mechanical L_{REA} values associated with the bulk modulus and shear modulus are significantly greater than that of the morphological L_{REA}, and (iii) the mechanical L_{REA} estimates of the shear modulus are greater than that of the

bulk modulus. Moreover, our study highlights that these qualitative results do not depend on the chosen micromechanical models and, thus, would be independent of the underlying anisotropic nature of shale.

Keywords: microstructure, shales, clay-rocks, anisotropy, clay, elastic properties.
Short title: Mechanical REA of shales inferred by micromechanics.

Highlights

- New estimates for the REA sizes of COx claystone and Tournemire argillite.
- Mechanical REA size is greater than morphological REA size.
- REA sizes of Tournemire argillite are greater than those of the COx map.
- REA sizes of shear modulus are greater than those of the bulk modulus.
- These results do not depend on the chosen micromechanical models.

1. Introduction

Clay rocks, often called shales, are being studied as potential host rocks for high-level radioactive waste repositories in several industrial countries (e.g., ANDRA, 2005; Pusch, 2006) and form the main geological caps of many hydrocarbon reservoirs (e.g., Aplin and Larter, 2005). Organic-rich clay rocks are considered to be the key petroleum source rocks for the coming decades (e.g., Klaver et al., 2015). These geological formations are highly heterogeneous at multiple scales, but a major proportion of the literature agrees that the following relevant microstructural levels must be considered (e.g., Bennett et al., 1991; Jakobsen et al., 2003; Ulm et al., 2005; Ortega et al. 2007; 2009; Bobko and Ulm, 2008; Loucks et al., 2012; Cariou et al., 2013; Keller, 2015) (Figure 1):

- Level 0 is the scale of elementary clay layers.
- Level 1 is the scale for which the elementary clay layers are packed together to form clay particles.
- Level 2 is the submicrometer scale, often called the "microscopic" scale of porous clay composites constituted in a mixture of clay particles or aggregates.
- Level 3, often called the "mesoscopic" scale in geosciences, is the scale where the characteristic size is in the submillimeter range. At this scale, the rock is considered to be a porous clay matrix mixed with a population of nonclayey grains (mainly quartz, carbonates and pyrite). This is the scale of the mineral maps used in this work.
- Level 4 is a lamina type that is associated with an alternation of clay-rich layers and non–clayey materials (mainly quartz and carbonates).

With regards to the complexity of this hierarchical organization, the prediction of the engineering properties of shale from its microstructure is clearly a challenging task. In the following work, we will focus on the mesoscopic scale for which numerous theoretical studies

have been devoted to the calculations of the engineering or effective properties (e.g., Jakobsen et al., 2003; Levin and Markov, 2005; Ulm et al., 2005; Giraud et al., 2007a, 2007b; Ortega et al. 2007; 2009; Cariou et al., 2013; Cosenza et al., 2015a,b). This mesoscopic scale is often considered the key scale for modeling the mechanical and transport behaviors of clay rocks involved in high-level radioactive waste repositories (Abou-Chakra Guéry et al., 2010; Robinet et al., 2007; 2012; Cariou et al., 2013). These effective properties, which are inferred by numerical upscaling techniques or by homogenization theories, are used as inputs for numerical codes, often based on the finite elements method, for engineering purpose.

All the upscaling or homogenization approaches used to estimate these effective properties are based on the paramount concept of the Representative Elementary Volume (REV), which is required to "separate" the following two space scales: the scale of heterogeneity, i.e., nonclayey grains (or rigid inclusions) in our case, and the scale of engineering for which clay rock is viewed as a continuum of homogeneous medium. Thus, the REV is usually considered as a volume of heterogeneous material that is sufficiently large to be statistically representative of the rock, i.e., to include a relevant sampling of all the microstructural heterogeneities existing in the rock at the scale of interest (here, the mesoscopic scale) (e.g., Kanit et al., 2003; Zhang et al., 2017). At the same time, the REV has to be small enough, compared to the scale of the macroscopic geotechnical systems of study, "so that it may be considered as infinitesimal in the mathematical treatment" (Biot, 1941).

To our knowledge, the approaches used to estimate the size of a REV, named hereafter L_{REV}, can be divided for the sake of simplicity into two groups that introduce the probabilistic concept of realization; here, a realization is any representation of the microstructure considered with a given size and a given fraction of heterogeneities. The first approach or group of approaches aims at using statistical parameters, e.g., mean, standard deviation or covariance, of a given geometrical or physical property (e.g., porosity, fraction of a given mineralogical phase,

mechanical property, etc.) calculated over a significantly large set of realizations to quantitatively describe the heterogeneous structure of the material of interest (Torquato and Stell, 1982; Zhang et al., 2000; Kameda et al., 2006; Houben et al. 2014; Klaver et al., 2015; Fauchille et al., 2018). Following these approaches, REV is defined as the elementary volume below which the property of interest varies significantly across the scale. Among these approaches, the "counting box" method and the covariance or the two-point probability function are likely the most popular and have been recently applied to 2D images acquired on shale samples (i.e., Pasidonia shale, Germany, Klaver et al., 2015; Callovo-Oxfordian argillites, France, Song et al., 2015; Opalinus clay, Switzerland, Keller et al., 2013; Houben et al. 2014; Bakken shale, United States of America, Liu and Ostadhassan, 2017; and Bowland shale, United Kingdom, Fauchille et al., 2018). It should be noted that most of these works have been performed on 2D images and, thus, provided estimations of the Elementary Representative Area (REA) size, hereafter named L_{REA}.

This first group of approaches is often referred to as "deterministic" approaches (Rolland du Roscoat, et al., 2007; Khdir et al., 2012), in contrast with a second group of approaches that explicitly introduce the concept of the "statistical" REV. Following Kanit et al. (2003) and Jeulin et al. (2004), a "statistical" REV is related not only to the microstructure and the physical properties of each components but, above all, to a given precision in the estimation of the effective property depending on the number of realizations "that one is ready to generate" (Jeulin et al., 2004). Consequently, in comparison with the aforementioned approaches, the "statistical" L_{REV} depends explicitly on an additional parameter, i.e., the precision desired for the estimate of the effective property and reached for a given number of realizations. Consequently, the estimate of the "statistical" L_{REV} cannot be unique without any associated precision and number of realizations. This statistical approach has been recently applied to

Opalinus clay samples taken from the Mont Terriç rock laboratory in Switzerland (Houben et al., 2014; Keller, 2015; 2016a,b).

In summary, this brief review shows that a large variety of methods used to infer L_{REV} or L_{REA} estimates with regard to shale exist, and these estimates concern mainly the petrographical or mineralogical parameters of the porosity and mineral phases. Most of them have been obtained by deterministic approaches, e.g., the counting box method and dispersion method based on the standard deviation calculations. Moreover, to our knowledge, estimates of the mechanical L_{REV}/L_{REA} of shales are very scarce; one recent and single work was performed on Opalinus clay by Keller (2016a,b), and it focused on the dynamic elastic moduli.

The objective of this paper is thus twofold. First, we would like to provide new estimates of L_{REA} obtained from two mineral maps (Jorand, 2006; Fauchille, 2015) acquired from two shales extensively studied in the framework of the deep disposal of radioactive waste, as follows: Callovo-Oxfordian (COx) claystone from the Meuse/Haute-Marne underground research laboratory (Eastern France) and Toarcian argillite from the experimental station of Tournemire (Southern France). These estimates have been obtained by the classical counting box method and the statistical approach promoted by Kanit et al. (2003; 2006) and Jeulin et al. (2004). Second, we would like to quantify the statistical mechanical L_{REA} of COx claystone and Tournemire argillites by focusing on static elastic parameters for further engineering purposes. These mechanical L_{REA} are inferred by using micromechanical approaches, one of which implicitly accounts for the transverse isotropic nature of shale.

2. Mineral maps

The L_{REA} estimates calculated in this study have been obtained from two mineral maps acquired following the methodologies described below.

The first mineral map, hereafter called the COx map, has been made from a sample taken from the Callovo-Oxfordian (COx) claystone, which is under extensive study at the

160 Meuse/Haute-Marne Underground Research Laboratory (MHM-URL) (Eastern France). The
161 thickness of this formation is 130 m and its age is 150-160 My; the formation is located 420-
162 550 m below the surface, in the eastern part of the Paris Basin (Andra, 2005). The Callovo-
163 Oxfordian formation contains mainly 25 to 65 wt.% clay minerals, with 20-42 wt.% carbonates
164 (calcite, dolomite, ankerite) and 15-31 wt.% quartz and feldspars (Andra, 2005). Considering
165 nonclay minerals, feldspars contents are negligible regardless to quartz. Among carbonates,
166 siderite and dolomite are negligible regardless to calcite. Thus, quartz and calcite will be the
167 only nonclay minerals considered in the following.

168 This mineral map was prepared from a drill-core, denoted as EST05-709 (-492.2 m) and
169 extracted from the Andra EST205 borehole (Jorand, 2006; Conil et al., 2018). It was obtained
170 at a micrometer spatial resolution from an advanced image processing of a chemical elements
171 map that was acquired through the use of a Cameca SX100 electron probe microanalyzer (Prêt,
172 2003). This electron microanalyzer provides quantitative concentration maps of 14 chemical
173 elements (Al, Na, K, Ca, Si, Mg, Ti, Fe, S, Ba, Zr, P, Zn, Sr) on a 3 x 0.5 mm^2 area with a
174 spatial resolution of 2 μm/pixel. The image processing of these maps is based on mineral
175 thresholding methods that accommodate mixtures and solid solutions. For details, the reader is
176 referred to Prêt (2003) and Prêt *et al*. (2010a,b). In our case, this methodology allows for the
177 spatial location of 16 different minerals, including the following three different clay minerals:
178 illite-smectite mixed layers, kaolinite and chlorite.

179 The geometrical and mineralogical features of the COx map are given in Table 1. The
180 surface fractions of the clay matrix, calcite and quartz are 50.4%, 25.0% and 13.8%,
181 respectively. Note that the largest side (1563 pixels, 3072 μm) and the smallest side (250 pixels,
182 500 μm) are perpendicular and parallel to the bedding, respectively.

183 The second mineral map, hereafter called the Toar map, has been extracted form a large
184 mosaic acquired from a nonimpregnated and dried Tournemire clay rock sample (Fauchille et

al., 2014; Fauchille, 2015). The Tournemire clay rock sample studied has been sampled in the horizontal and cylindrical borehole FD90 in the 1996 East gallery of the Tournemire Underground Research Laboratory (URL) of the French Institute for Radioprotection and Nuclear Safety (IRSN). The sample was located at a depth between 4.20 to 4.40 meters far from the gallery wall, outside the so-called Excavation Damaged Zone. The Tournemire URL is located in a Mesozoic basin on the southern border of the Massif Central (Aveyron, France), in the subhorizontal consolidated argillaceous Toarcian formation (200 meters thick) and marly layers of the Domerian age (50 meters thick). The sample comes from the upper Toarcian formation, whose mineralogical composition shows that clay minerals represent nearly 25-70 wt% of the rock with illite (10-40 wt%) and illite/smectite mixed-layer minerals (5-25 wt%), kaolinite (10-35 wt%) and chlorite (1-5 wt%). The Tournemire clay rock also contains 10-40 wt% of carbonates, 10-30 wt% of quartz, 2-7 wt% of sulfides and less than 2 wt% of feldspars (Cabrera et al., 2001). Similarly to COx map, quartz and calcite are the dominant nonclay minerals and will be the only nonclay minerals to be considered.

The mosaic of interest (7.1 x 5.2 mm², 11302 x 8355 pixels) has been built from one hundred and fifty three back-scattered electron images (spatial resolution of 0.625 µm.pixel^{-1}) acquired by Scanning Electron Microscopy (SEM, JEOL JSM 56000LV with an acceleration voltage of 15 kV, a probe current of 5 nA, a working distance of 16.3 mm, a magnification of x200, and a dwell time of 128 µs per pixel). On the mosaic of images, the clay-matrix, carbonates, quartz, sulfides and macropores were differentiated by the MicroPhaseMap© software developed at the IC2MP laboratory in Poitiers, allowing the boundary between the clay matrix and nonclay grains to be determined (Prêt et al., 2010a,b). The mineral map used in this study concerns an extraction (4000x4000pixels) of the most homogeneous part of the mosaic in order to respect at best the statistical homogeneity assumed in all the further L_{REA} calculations. The geometrical and mineralogical features of this map are also given in Table 1.

Extractions of both maps are given in Figures 2 and 3. Note that both maps were prepared from a polished thin section in a plane perpendicular to the stratigraphic plane. The x-direction indicated in Figures 2 and 3 is parallel to the bedding planes, whereas the z-direction is perpendicular to the bedding.

The results of these image analyses are given in numerical files in which the location and mineral code of each pixel of the mineral maps are indicated. These numerical files are the input files for the L_{REA} estimate calculations that are presented in the next section.

3. Methodologies used to infer the REA size

3.1 Counting box method

The counting box method, which is likely the most popular to infer L_{REA}, starts from a given subdomain or box in the digitalized image. Then, the mean of a surface property (surface mineral contents, surface porosity, physical property, etc.) is calculated within increasing subdomains, often called boxes, until the actual image size is reached (Houben et al., 2014; Klaver et al., 2015). The characteristic size L_{REA} is considered to be reached when the mean of the considered property does not evolve significantly with the increasing size of boxes. This procedure can be repeated for several starting subdomains to make sure that the inferred L_{REA} is statistically representative of the whole image. This first method will be named hereafter the classical counting box (CB) method.

Regarding the use of square domains in the CB method, the COx and the Toar maps have been divided into six and four nonoverlapping square areas, respectively, following the partitioning given in Figure 4. These nonoverlapping areas, named Ai (i=1,..,6 for COx map; i=1,..,4 for Toar map), are associated with the starting of the subdomains, which are defined and discriminated by the coordinates of their center Ci (i=1,..,6 for COx map; i=1,..,4 for Toar map) (Figure 4). Note that the origin, i.e., x=0, z=0 of the system of coordinates is located in the top left corner of both maps (Figures 2, 3 and 4).

The particular partitioning displayed in Figure 4 is due to two reasons. First, the shape of the COx map is elongated following the z-axis and the center of the initial box could not be located only at the center of this map to investigate the whole map. Second, it was interesting from a statistical viewpoint to compare the L_{REA} estimates calculated at different areas with a comparable surface and, thus, to check the statistical homogeneity of each map. Note that the number of pixels of each area is sufficient to apply the deterministic CB approach.

3.2 "Statistical" Elementary Representative Area (REA)

Kanit et al. (2003; 2006) and Jeulin et al. (2004) extended the classic definition of REV by explicitly integrating the concept of "desired precision" into the calculated effective property. Following their approach, the effective physical properties of heterogeneous materials can be determined not only by one single numerical simulation on a large volume (greater than the REV) of the microstructure but also as the mean value of apparent properties calculated on volumes smaller than the REV, provided than a sufficient number of realizations of the microstructure are considered (e.g., Rolland du Roscoat et al., 2007). Therefore, the "statistical" REV introduced in this manner is not unique; it is defined as a function of the physical properties of each component, the microstructure, the desired precision and the number of realizations. This methodology was used to determine the "statistical" REVs of mechanical and thermal properties of specific random microstructures (Kanit et al., 2003; Pelissou et al., 2009) and of real microstructures of clay rock (Houben et al., 2014; Keller, 2015; 2016a,b). In our study, we will focus on elastic moduli of shale considered as a transverse isotropic rock.

The determination of "statistical" REVs is obtained following a two-step procedure. In the first step, the paramount concept of this approach, the integral range A_3 (or A_2 by considering a 2D image) has to be evaluated.

3.2.1 Determination of integral range

Considering a 2D microstructure, the integral range A_2, which depends on the studied property, is directly related to the scatter (the dispersion) in apparent properties calculated from several realizations *n* of the microstructure of fixed size *S*. The integral range gives information on the area size of the microstructure, for which the property measured in this area has a convenient statistical representativity (e.g., Matheron, 1971; Lantuéjoul, 1991).

For an ergodic, stationary random function *Z(x)*, and for a large specimen ($S>>A_2$), the integral range A_2 can be obtained by the following expression (appendix; see also Lantuéjoul, 1991; Kanit et al. 2003; 2006 and Jeulin et al., 2004) as follows:

$$D_Z^2(S) = D_Z^2 \frac{A_2}{S} \quad (1)$$

where $D_Z^2(S)$ is the variance of the mean value $\bar{Z}$ over the surface *S* and D_Z^2 is the point variance of *Z(x)*. Equation (1) is valid for additive properties (e.g., surface fraction or mass density) and, thus, can be rewritten as follows when the surface clay fraction, namely, φ, is considered:

$$D_\varphi^2(S) = \bar{\varphi}(1-\bar{\varphi}) \frac{A_2}{S} \quad (2)$$

where the variance D_Z^2 is $\bar{\varphi}(1-\bar{\varphi})$. As the composition of a physical property *Z(x)* (e.g., elastic moduli in our case) in the change of scale is not additive, the latter relation (2) is no more valid, and Kanit et al. (2003) proposed the following modified version:

$$D_Z^2(S) = D_Z^2 \left(\frac{A_2}{S}\right)^\alpha \quad (3)$$

where α is an exponent that has to be determined. In the case of a two-phase material with the physical property Z_1 for phase 1 and Z_2 for phase 2, the point variance of the random variable *Z* is as follows (Kanit et al. 2003; and Jeulin et al., 2004):

$$D_Z^2 = P(1-P)\,(Z_1 - Z_2)^2 \quad (4)$$

where *P* is the volume fraction of phase 1 or phase 2. In practice, phase 1 and phase 2 are the clay matrix and nonclay inclusions, respectively. In this study, this means that properties

283 Z_1 and Z_2 are the elastic modulus, either the bulk modulus or shear modulus, of the nonclay
284 inclusions and clay matrix, respectively.

285 As illustrated further, in both cases, i.e., considering the clay fraction φ (equation 2) and
286 a chosen physical property Z (equation 3), the integral range A_2 is obtained by fitting from the
287 graph of the function $D_\varphi^2(S)$ or $D_Z^2(S)$. In our case, let us recall that Z is an elastic modulus,
288 either the bulk modulus or shear modulus, the variance $D_Z^2(S)$ of which is calculated on the
289 partitions of the mineral map in subdomains of a given area S. The value of Z for a given
290 subdomain of area S is obtained from the micromechanical approaches presented in the
291 following section 3.2.2.

292 *3.2.1 Determination of the REA size*

293 In a second step, the determination of the integral range allows the calculation of the
294 precision desired to estimate the size L_{REA}. In the theory of samples, the absolute error ε_{abs} and
295 the relative error ε_{rel} of the mean effective value $\bar{Z}$ obtained with n independent realizations of
296 area S are deduced from the interval of confidence as follows (e.g., Jeulin et al., 2004):

297 $$\varepsilon_{abs} = \frac{2\, D_Z(S)}{\sqrt{n}} \quad (5)$$

298 $$\varepsilon_{rel} = \frac{\varepsilon_{abs}}{\bar{Z}} = \frac{2\, D_Z(S)}{\bar{Z}\sqrt{n}} \quad (6)$$

299 Thus, the REA area, S_{REA}, can now be defined as the area for which n realization ($n=1$
300 for instance) is required to estimate the mean effective property $\bar{Z}$ with a given relative error
301 ($\varepsilon_{rel}=5\%$ for instance) provided that the function $D_Z(S)$ is known.

302 For instance, if Z is the surface clay fraction named φ, the parameter S_{REA}, estimated
303 with a given relative error ε_{rel} and a given number of realization n, can be obtained by combining
304 equations (6) and (2), as follows, provided that the mean effective property $\bar{\varphi}$ is known:

305 $$S_{REA} = L_{REA}^2 = \frac{4(1-\bar{\varphi})A_2}{n\, \varepsilon_{rel}^2\, \bar{\varphi}} \quad (7)$$

In the same way, if Z is now a physical property, the corresponding parameter S_{REA}, estimated with a given relative error ε_{rel} and a given number of realization n, can be deduced by combining equations (3), (4), (5) and (6), as follows, provided that the mean effective property $\bar{Z}$ is known:

$$S_{REA} = L_{REA}^2 = \left[\frac{4P(1-P)}{n\,\varepsilon_{rel}^2}\frac{(Z_1 - Z_2)^2}{\bar{Z}^2}\right]^{1/\alpha} A_2 \qquad (8)$$

At this stage, two remarks have to be formulated. First, the integral range A_2 in both equations (7) and (8) are not *a priori* similar. The integral range A_2 depends on the property under study, i.e., φ or Z, and has to be evaluated separately. Second, this approach assumes that the mean effective properties $\bar{\varphi}$ and $\bar{Z}$ are known *a priori*. In practice, the latter are calculated on macroscopic areas supposed to be much greater than the area of the REA.

In summary, a "statistical" REV is therefore determined with the following algorithm (Kanit et al., 2003):

i) Consider different realizations of the microstructure, i.e., different partitions of the mineral map in subdomains of a given area S.

ii) Calculate the mean and the variance of the property of interest of the whole set of partitions under consideration; the graph of the function $D_\varphi^2(S)$ or $D_Z^2(S)$ is thus obtained.

iii) Estimate the integral range A_2 from the previous graph, equation (2) or equation (3) (in the later, the exponent α has to be evaluated as well).

iv) Define the precision ε_{rel} and the number of realization n to estimate the effective property of interest and calculate the L_{REA} with equation (7) or equation (8). The value of the effective property, $\bar{\varphi}$ or $\bar{Z}$ in equation (7) or equation (8), is independently estimated.

330 *3.3.2 Calculations of apparent elastic properties*

331 As mentioned previously, the calculation of the integral range A_2 associated with a given
332 mechanical property requires the values of the average and the variance of the mechanical
333 property calculated over a set of subdomains of the map of interest (step ii). This means that
334 the mechanical property under study has to be calculated in each subdomain of size S of the
335 map partition. The apparent mechanical property associated with a given subdomain has been
336 estimated in this work by two micromechanical approaches.

337 *Anisotropic model*

338 Following the first micromechanical approach, hereafter called the anisotropic model,
339 the transverse isotropic nature of shale is implicitly taken into account. This anisotropic model
340 is itself achieved in two steps. In a first step, the apparent anisotropic stiffness tensor in the
341 subdomain of interest is calculated by an inclusion-based model, i.e., a nonclay spherical grain
342 embedded in a clay transverse isotropic matrix following a differential effective medium
343 (DEM) scheme (e.g., Cosenza et al., 2015b). The latter scheme is widely and successfully used
344 in rock physics to model the elastic wave velocities of numerous rocks (e.g., Hornby et al.,
345 1994; Markov et al., 2005).

346 The DEM scheme consists of iteratively adding spherical inclusions with diluted
347 concentration into the current effective medium determined in the previous step. At the initial
348 stage, a material with elastic moduli $\boldsymbol{C_M}$ is considered as the initial host material. A dilute
349 concentration of spherical inclusions is then added into this initial host; the effective tensor of
350 this new composite can be calculated without considering the interactions between the
351 inclusions. The construction process continues as follows: (a) at each stage, the embedded
352 spherical inclusions are scattered in diluted concentration and (b) the required volume fraction
353 of inclusions is satisfied. At a given step, indexed i, the small increment of stiffness due to the
354 addition of a small fraction of inclusions, df_i is given by the following:

$$d\boldsymbol{C}_i^{ap} = \frac{df_I}{1-f_I}\left(\boldsymbol{C}_I - \boldsymbol{C}_i^{ap}\right): \left[1 + \boldsymbol{P_i}: \left(\boldsymbol{C}_I - \boldsymbol{C}_i^{ap}\right)\right] \quad (9)$$

This increment $d\boldsymbol{C}_i^{ap}$ must be added to the apparent tensor $\boldsymbol{C}_i^{ap}$ obtained in the previous step. Note that the bold capital letters refer here to fourth-order tensors. In our case, the stiffness tensors $\boldsymbol{C_I}$ and $\boldsymbol{C_M}$ are the stiffness tensor of the isotropic nonclay sphere and the stiffness tensor of the transverse isotropic clay matrix, respectively. The Hill's tensor $\boldsymbol{P_i}$ is a function of $\boldsymbol{C}_i^{ap}$ and the Eshelby's tensor, which depends on the chosen inclusion-based model, as follows:

$$\boldsymbol{P}_i = \boldsymbol{S}_i: \left(\boldsymbol{C}_i^{ap}\right)^{-1} \quad (10)$$

The expressions of components of the Hill's tensor for a spherical inclusion in a transversely isotropic medium have been taken form Withers (1989) and Giraud et al. (2007a,b).

In a second step, the apparent tensor $\boldsymbol{C}^{ap}$ obtained by DEM is isotropized following the classical decomposition, as follows:

$$\boldsymbol{C}^{ap,is} = 3K^{is}\boldsymbol{J} + 2\mu^{is}\boldsymbol{K} \quad (11)$$

with

$$K^{is} = \frac{\boldsymbol{C}_J^{ap,is}}{3} = \frac{\boldsymbol{J}::\boldsymbol{C}^{ap}}{3} \; ; \mu^{is} = \frac{\boldsymbol{C}_K^{ap,is}}{10} = \frac{\boldsymbol{K}::\boldsymbol{C}^{ap}}{10} \quad (12)$$

$$\boldsymbol{C}_J^{ap,is} = \frac{1}{3}\boldsymbol{C}_{iijj}^{ap,is}; \boldsymbol{C}_K^{ap,is} = \boldsymbol{C}_{ijij}^{ap} - \frac{1}{3}\boldsymbol{C}_{iijj}^{ap,is} \text{ (summation on repeated indices i,j)} \quad (13)$$

and four-rank tensors $\boldsymbol{J}$ and $\boldsymbol{K}$ obey the following algebraic properties:

$$\boldsymbol{J}:\boldsymbol{J}=\boldsymbol{J} \; ; \; \boldsymbol{K}:\boldsymbol{K}=\boldsymbol{K} \; ; \; \boldsymbol{K}:\boldsymbol{J}=\boldsymbol{J}:\boldsymbol{K}=0 \quad (14)$$

With

$$J_{ijkl} = \frac{1}{3}\delta_{ij}\,\delta_{kl} \; ; I_{ijkl} = \frac{1}{2}(\delta_{ik}\delta_{jl} + \delta_{il}\,\delta_{jk}) \; ; K_{ijkl} = I_{ijkl} - J_{ijkl} \quad (15)$$

This "isotropization" process of apparent stiffness tensor $\boldsymbol{C}^{ap}$ is due to two reasons. The first reason is theoretical. The original methodology described in Kanit et al. (2003; 2006) and Jeulin et al. (2004) involves the isotropic physical properties in equations (3), (4) and (8). We do not know to what extent this methodology can be generalized to anisotropic media, i.e., to

mixtures of anisotropic constituents. In other words, this generalization to anisotropic media has to be proven and its demonstration is beyond the scope of this work. Moreover, it should be noted that despite this "isotropization" process, the calculation of the apparent stiffness tensor of shale is impacted by that of the anisotropic stiffness tensor of the clay matrix and, thus, implicitly depends on the anisotropic nature of rock. The second reason is methodological. This "isotropization" allows the following results to be directly compared to those obtained by a pure isotropic model presented further, since both models provide apparent moduli with the same physical meaning.

Equations (11) to (15) allow the extraction of the apparent isotropized bulk modulus, K^{is} and the apparent isotropized shear modulus μ^{is}, which are used to infer the statistical mechanical REA sizes (i.e., using equation (8)). However, the calculations of K^{is} and μ^{is} and, thus, the $\boldsymbol{C}^{ap}$ components require input data, which are the components of the stiffness tensors $\boldsymbol{C_I}$ and $\boldsymbol{C_M}$.

The components of stiffness tensor $\boldsymbol{C_I}$ correspond to the elastic moduli of nonclay grains (quartz and calcite) whose values have been taken from Mavko et al. (2009). In our calculations, the isotropic elastic moduli of the nonclay phase, i.e., the bulk and shear modulus, are the weighted averages of those of quartz and calcite, where the weights are the gravimetric contents of each phase, as indicated in Table 2. In fact, the pure calcite and quartz phases are anisotropic minerals (e.g., Mavko et al., 2009); their isotropized equivalent elastic properties considered here correspond to random distributions in the orientation and the space of calcite and quartz inclusions (e.g., Ulm et al., 2005; Giraud et al., 2007b).

The elastic moduli of the clay matrix are more difficult to estimate, because the clay phase is also a heterogeneous composite composed of aggregates of clay layers, pores filled with interstitial fluids and, likely, fine nonclay minerals (Figure 1). Consequently, in practice, the elasticity of the clay phase is complex, which makes it difficult to quantitatively characterize

in an experimental viewpoint, and, thus, is poorly constrained in our context. To our knowledge, the most relevant range of transverse-isotropic elastic properties of a clay matrix at the mesoscopic scale has been obtained by Ulm et al. (2005), who used an experimental micromechanics approach by combining nanoindentation measurements with the microporoelasticity theory. These authors have proposed quantitative estimations of elastic moduli, which resulted from the inversion of nanoindentation measurements obtained on three different shale materials at spatial scales of 10^{-7} to 10^{-5} m, which correspond to that of our mineral maps (Ulm et al., 2005; Cosenza et al., 2015b). In our calculations, only the lower bound of the range proposed by Ulm et al., (2005) has been considered (Table 2). Indeed, the values of transverse isotropic moduli considered in Table 2 provided mean values of apparent elastic moduli that are the closest to the reference macroscopic elastic moduli measured in both shales under study. Higher values of clay elastic moduli would have led to much higher values of apparent moduli that are significantly higher than the experimental elastic moduli measured on both shales.

Isotropic model

In the second micromechanical approach used in this work, hereafter called the isotropic model, the elastic properties of the clay matrix, K_M and μ_M, were not given *a priori*. They have been inverted following a Monte-Carlo procedure to overcome the paramount difficulty of quantitatively characterizing the clay phase elasticity. This inversion procedure has considered the following as input data: the weighted averages of quartz and calcite, the elastic properties of both shales and the reference macroscopic elastic properties, which are all given in Table 2. It was based on a simple micromechanical model, i.e., an inclusion-based model consisting of an isotropic sphere embedded in an isotropic matrix. This isotropic inclusion-based model corresponded again to a DEM approach, which is expressed by the following coupled differential equations (e.g., Christensen, 2012):

$$dK^{ap} = \frac{df_I}{1-f_I}\,\frac{K_I - K^{ap}}{1+\frac{K_I - K^{ap}}{K^{ap}+4/3\mu^{ap}}} \quad (16)$$

$$d\mu^{ap} = \frac{df_I}{1-f_I}\,\frac{15(1-\nu^{ap})(\mu^{ap}-\mu_I)}{7-5\nu^{ap}+2(4-5\nu^{ap})\frac{\mu_I}{\mu^{ap}}} \quad (17)$$

with

$$\nu^{ap} = \frac{3K^{ap}-2\mu^{ap}}{2(3K^{ap}+\mu^{ap})} \quad (18)$$

The Monte-Carlo procedure consisted of 10000 random trials of clay matrix moduli ranging between 0 GPa and the reference macroscopic values given in the first column in Table 2. The maximum relative difference between the reference macroscopic value and the calculated macroscopic value by our inverse procedure was less than 2% (Table 3). This difference was considered acceptable with regard to the high uncertainty associated with the quantification of clay matrix elastic moduli.

4. Results and Discussion

4.1 Counting box REA sizes versus Statistical morphological REA sizes

REA sizes inferred by the counting box method

Figures 5 and 6 display the evolutions of the clay fraction calculated on increasing box sizes *L* considering the different starting domains of the COx map and Toar map, respectively. Both figures confirm that the calculated clay fraction is a decreasing function of *L* and converges to a value, hereafter referred to as the parameter φ_∞, which is very close to the mean clay fraction obtained on the whole map (Table 1).

Considering the COx map (Figure 5a.), the six curves associated with six starting domains converge to φ_∞values in the range [48.6-52.4%], including the mean clay fraction $\overline{\varphi}_{COx}$ of 50.4% calculated on the whole map (Table 1). The difference between these asymptotic values, φ_∞, and the mean clay fraction $\overline{\varphi}_{COx}$ is less than 4%. In the same way, in Figure 5b, the

four curves associated with the Toar map converge to φ_∞ values in the range [68.5-71.4%], which also include the mean clay fraction $\overline{\varphi}_{Toar}$ of 69.9% calculated for the whole map (Table 1). The difference between the φ_∞values and $\overline{\varphi}_{Toar}$ is less than 2.5%.

Below 100µm and 200µm for COx and Toar maps respectively, the curves obtained for the different subdomains presents non correlated and high frequency evolutions. Such a behavior is associated to the occurrence of a few grains with such a large size (Robinet, 2008; Fauchille, 2015) and that large enough box size including several grains should be used to estimate a meaningful REA (Gaboreau et al 2016). For larger box size than 100µm and 200µm for COx and Toar maps respectively, the gap between the curves decreases progressively with low frequency variations. Meaningful REA corresponding to mesoscopic scale (level 3 in Figure 1) could be estimated with an improved accuracy when the box size increases. The careful observation of both maps reveals that grain size is larger for Toar than for COx (compare calcite grains in Figure 2 and carbonates grains in Figure 3), somehow explaining why a larger box size is needed for Toar map to reach a REA as illustrated below (Figures 5a and 5b).

The REA size, i.e., L_{REA}, of both maps has been estimated in two steps (Table 4). In the first step, the REA sizes have been calculated for each of the nonoverlapping areas of both maps (6 areas for the COx map and 4 areas for the Toar map) and for two errors or threshold values, i.e., ε= 0.1 (10%) and ε= 0.05 (5%). For each area, the L_{REA} parameter has been identified as the lowest box size L for which the calculated mean clay fraction was significantly similar to that of the whole map ($\overline{\varphi}_{COx}$ or $\overline{\varphi}_{Toar}$), with a maximum error of ε. In a second step, the average overall L_{REA} estimates of all nonoverlapping areas have been calculated for each map. The calculated mean L_{REA} for a given map has been considered as the L_{REA} of the latter.

Our results given in Table 4 indicate that the L_{REA} values are dispersed and decreasing functions of the chosen error or threshold values ε. Indeed, in the first case (ε=0.1), the mean values of the L_{REA} estimates of the COx map and Toar map are 173 µm and 129 µm, respectively

475 (Table 2). Whereas in the second case (ε=0.05), the mean values of the L_{REA} estimates of the
476 COx map and Toar map are much higher, i.e., 234 µm and 441 µm, respectively.

477 This scatter in the L_{REA} estimates can also be evidenced by a calculation of the standard
478 deviation of the L_{REA} estimates associated with nonoverlapping areas (Table 4). Considering the
479 COx map, the standard deviation values of the L_{REA} estimates increase from 108 µm (ε=0.1) up
480 to 143 µm (ε=0.05). The standard deviation values of the L_{REA} estimates of the Toar map
481 increase from 72 µm (ε=0.1) up to 267 µm (ε=0.05) (Table 4).

482 This scatter questions the statistical homogeneity of both maps and could be explained
483 by a small but significant evolution of the microstructure in the x direction and/or in the z
484 direction (i.e., with depth); this is shown in (a), where the φ_∞, estimates of the COx map,
485 globally increase with depth, and by (b), where the φ_∞ estimates of the Toar map, decrease in
486 the x direction (Table 4).

487 However, the order of magnitude of all these estimates is comparable to the results from
488 other shales obtained also by the CB method (Opalinus clay: 180-250 µm, Houben et al., 2014;
489 Posidonia shale and Whitby shale: 200 µm, Houben et al., 2016; Bowland shale: 380 µm, Ma
490 et al., 2016; Bakken shale: 176 µm, Liu and Ostadhassan, 2017).

491 *Statistical morphological REA sizes*

492 Figure 6 displays the mean values of the surface clay fraction $\bar{\varphi}$ and their corresponding
493 standard deviation values, all calculated on sets of map partitions in subdomains of size L
494 ranging from 6 to 140 µm (COx map) and from 6.25 to 250 µm (Toar map). Note that these
495 sets of map partitions do not correspond to the partitions Ai indicated in Figure 4, which have
496 only been used for the CB method. All estimates of the statistical REA sizes in the following
497 have been obtained by considering the whole maps.

Figure 6 suggests the following two comments. First, whatever the subdomain size, the mean values of the surface clay fraction (50.5% for COx map and 69.9% for Toar map) are very close to that of the whole map ($\overline{\varphi}_{COx}$ or $\overline{\varphi}_{Toar}$). For large subdomain sizes, these mean values are almost equal to $\overline{\varphi}_{COx}$ or $\overline{\varphi}_{Toar}$. Second, the dispersion of the results characterized by their standard deviation decreases with increasing the subdomain size and tends to a plateau for L values approximately equal to 100 µm and 140 µm, considering the COx map and the Toar map, respectively (Figure 6). Both trends are similar to those already observed for other materials, considering other microstructural properties (porosity and specific surface area) (Zhang et al., 2000; Kanit et al., 2003, 2006).

The decrease in dispersion with L for both maps evidenced in Figure 6 is also illustrated in Figure 7, which displays the evolution of the pseudovariance $D_{\varphi}^{2}(S)/(\bar{\varphi}(1-\bar{\varphi}))$ as a function of the subdomains area S (i.e., L^2). In Figure 7, a 1/S fit for a large S by the least-square method is also indicated to obtain values of the integral range A_2 (equation (2)) required to calculate estimates of the REA size, $L_{REA,}$ for both maps (equation (7)).The results of the fits for both maps and the L_{REA} estimates considering one realization (n=1) and a range of error [5-10%] are given in Table 5. This table shows two results.

First, the L_{REA} estimates in Table 5 are rather close to those obtained by the CB method with similar values of errors, i.e., between 5 and 10% (Table 4). Indeed, in the case of the COx map, the statistical REA size, L_{REA}, is in the range of [205-410 µm], whereas L_{REA}, estimated by CB method is in the range of [50-438 µm] (Table 4). In the case of the Toar map, the statistical L_{REA} estimates are in the range of [345-696 µm], whereas the L_{REA} estimates by the CB method are in the range of [68-749 µm]. However, the comparison between these two types of estimate is no more relevant for smaller errors ε since the L_{REA} estimate inferred by the statistical method drastically increases as a function of 1/ε (see equation (10)).

Second, whatever the ε value, these results demonstrate that the REA size of the Callovo-Oxfordian claystone is lower than that of the Tournemire argillite. The REA size estimates of the COx map are in the range of [205-410 μm], whereas those of the Toar map are in the range of [345-696 μm]. This hierarchy has also been observed in Table 4 following the CB method applied with a ε value of 5%.

Figure 8 displays the values of the statistical morphological REA size, $L_{REA,}$ as a function of error ε(%) for one realization (n=1) for both mineral maps. The gray area in Figure 8 indicates the L_{REA} estimates for errors in the range of [0.1-10%]. Figure 8 shows that the L_{REA} estimates of the COx map are always lower than those of the Toar map, regardless of the ε values.

4.2 Statistical morphological REA sizes versus Statistical mechanical REA sizes

Figures 9a and 9b display the evolution of the mean values of the mechanical moduli (bulk modulus and shear modulus) considering both the anisotropic and isotropic models as a function of the size L of subdomains S. These figures confirm two trends previously observed in Figure 6. First, the mean values $\overline{K}$ and $\bar{G}$ tend rapidly towards plateaus which are close to the reference values for large S. These asymptotic values depend on the micromechanical model, i.e., the anisotropic or isotropic model used to calculate the mean values $\overline{K}$ and $\bar{G}$. Second, the dispersion of the results decreases again with an increasing subdomain size. In addition, Figures 9a and 9b show that whatever the micromechanical used, the mean values $\overline{K}$ and their associated dispersion (through standard deviation values) are always greater than the mean values $\bar{G}$ and its associated dispersion.

The decrease in dispersion with L for both maps evidenced in Figures 9a and 9b can also be illustrated in Figures 10a and 10b, which display the evolutions of the variance of elastic moduli as a function of the subdomains area S (i.e., L^2). Figures 10a and 10b also show that the power fit introduced by equation (3) is a relevant model to quantitatively describe these

547 dispersion evolutions and, hence, to determine the integral range; the calculated regression
548 coefficient R^2 values are all greater than 0.99. For each map, the parameters of these fits,
549 especially the exponents are very close (COx map: 0.89 to 0.896 for the bulk modulus and 0.983
550 to 1.026 to the shear modulus; Toar map: 0.83 for the bulk modulus and 0.813 to 0.824 to the
551 shear modulus), which illustrates the fact that the calculated variances are of the same order of
552 magnitude for any micromechanical model and any elastic modulus under study. Moreover,
553 Figure 10b shows that the variances of the elastic moduli of the Toar map are almost
554 independent of the chosen micromechanical model.

555 Figures 11a and 11b show the mechanical L_{REA} values inferred from the calculations of
556 integral range values obtained from Figures 10a and 10b and equation (8). These figures
557 highlight at least three results. First, in the case of both mineral maps under study, these figures
558 show that for any micromechanical model and any elastic modulus under consideration, the
559 mechanical L_{REA} is significantly greater than morphological L_{REA} (compare Figures 11a and 11b
560 to Figure 8). The concept of L_{REA} fundamentally depends on the property of interest. Second,
561 all things being equal, the mechanical L_{REA} estimates of the COx map are lower than those of
562 the Toar map (see also Table 6). This hierarchy previously observed for the morphological L_{REA}
563 estimates (see Figure 8) is retrieved when the mechanical properties are considered. Third, for
564 any mineral map and any micromechanical model, the L_{REA} estimates of the bulk modulus are
565 lower than those of the shear modulus (Table 6). However, this difference between both
566 estimates is more tenuous in the case of the Toar map for which L_{REA} estimates for a given ε
567 value can be considered as similar and insensitive to the chosen micromechanical models in a
568 first order approach (Table 6).

569 *4.3 Impacts of anisotropy and heterogeneity at the map scale*

570 The calculations of different L_{REA} in this study are based on equations (7) and (8), which
571 *a priori* assume an isotropy of mechanical properties of interest. In this framework, the well-

572 known anisotropic nature of shale raises a difficulty that has been bypassed here by
573 “isotropizing” the transverse isotropic stiffness tensor of the clay matrix. Moreover, to study
574 the impact of this underlying anisotropy introduced in this manner, a pure isotropic
575 micromechanical model has been introduced for comparison purposes. Thus, the main objective
576 associated with the introduction of an implicit anisotropic model and a pure isotropic model
577 was to address the following question: what is the impact of the underlying mechanical
578 anisotropy of shale on its L_{REA} estimates?

579 All the outcomes provided by this work show that the following qualitative results do
580 not depend finally on the chosen micromechanical models and, thus, would be independent of
581 the underlying anisotropic nature of shale. These outcomes are as follows: (i) The mechanical
582 L_{REA} estimates are greater than the morphological ones; (ii) The mechanical L_{REA} estimates of
583 the Toar map are greater than those of the COx map; and (iii) The mechanical L_{REA} estimates
584 of the apparent shear modulus are greater than those of the bulk modulus.

585 The second underlying assumption used in this work is the statistical homogeneity of
586 both mineral maps, meaning, from a statistical viewpoint, that the stationarity assumption of
587 the properties of interest is satisfied on both maps (see appendix and Lantuéjoul, 1991;
588 Torquato, 2013). Let us recall that the stationary assumption means here that the statistical
589 properties implied in our calculations are invariant by translation, i.e., they do not depend on
590 the absolution position in the mineral maps. In our case, the L_{REA} estimated by the CB method
591 strongly depends on the starting domain chosen in the mineral maps, as shown by the high
592 values of standard deviation of the calculated mean L_{REA} values (Table 4). This strong spatial
593 variability of the L_{REA} estimate is a serious indication that the stationarity assumption would not
594 be fulfilled. This indication seems to be confirmed at least for the Toar map by the statistical
595 approach promoted in this study. Figure 12 clearly shows that the 1/S fit associated with
596 equation (2) is finally in poor agreement with the calculated pseudovariance of the clay fraction

used to calculate the integral range A_2 (coefficient of determination R^2 equal to 0.36). According to Lantuéjoul (1991), a poor agreement between equation (2) and the measurements would indicate that the image under study would not satisfy the stationary assumption. This result suggests that a combined use of the simple CB method and a calculation of the integral range following the statistical approach applied here would be a simple and efficient way to check *a posteriori* the statistical homogeneity of the maps and images under study at the mesoscopic scale, which is scarcely ensured in practice. This suggestion and these results have to be obviously verified on other mineral maps.

5. Concluding remarks

The main objective of this work was to provide new estimates of REA sizes of the following two shales actively studied in the framework of the deep disposal of radioactive waste: Callovo-Oxfordian (COx) claystone from the Meuse/Haute-Marne underground research laboratory (Eastern France) and Toarcian argillite from the experimental station of Tournemire (Southern France). The L_{REA} estimates obtained from two mineral maps at a mesoscopic scale have been calculated by the classic counting box (CB) method and a statistical approach that introduces the concept of a "statistical" REA. Following this approach, a "statistical" REA is related not only to the microstructure and the properties of each of the components but, above all, to a given precision in the estimation of the effective property depending on the number of realizations "that one is ready to generate" (Jeulin et al., 2004). The probabilistic concept of realization here is any representation or observation of the microstructure considered with a given size and a given fraction of heterogeneities, i.e., in our case, from a practical viewpoint, a subdomain of a given area of a mineral map. This statistical approach requires the calculations of the apparent elastic moduli in this subdomain or in the set of subdomains, which have been achieved here by using two micromechanical models. The first micromechanical model consisted of an anisotropic inclusion-based model for which

622 spherical nonclay grain is embedded in a clay matrix, in which the values of its transverse
623 isotropic stiffness tensor have been taken from literature. The second micromechanical model
624 was an isotropic inclusion-based model for which spherical nonclay grain is embedded in a
625 clay matrix; the elastic moduli values have been inverted by a Monte-Carlo approach from the
626 macroscopic engineering moduli measured on both shales under study. The calculations
627 performed following this statistical approach have shown the following results:

628 • The morphological L_{REA} estimates inferred for the statistical approach are of the
629 same order of magnitude as those found in the literature and obtained by the
630 classic CB method by considering the values of the relative errors, i.e., between
631 5 and 10%.

632 • For any micromechanical model and any elastic modulus under consideration,
633 the mechanical L_{REA} is significantly greater than morphological L_{REA}. Our study
634 confirms that the concept of L_{REA} fundamentally depends on the property of
635 interest.

636 • The mechanical L_{REA} estimates of the Toar map are greater than those of the COx
637 map. This is also the case for the morphological L_{REA} estimates inferred for a
638 low relative error of 5%.

639 • All things being equal, the mechanical L_{REA} estimates of shear modulus are
640 greater than those of the bulk modulus

641 Moreover, our study highlights two additional aspects. First, all the outcomes provided
642 by this work show that these previous qualitative results do not depend on the chosen
643 micromechanical models and, thus, would be ultimately independent of the underlying
644 anisotropic nature of the shale. Second, a combined use of the simple CB method with a
645 calculation of the integral range following this statistical approach strongly brings into question
646 the statistical homogeneity of the Toar map. Consequently, this result suggests that this coupled

approach would be a simple and efficient way to check *a posteriori* the statistical homogeneity of the maps and images under study, which is scarcely ensured in practice. The application and validation of such a coupled approach on other mineral maps is obviously one natural perspective of this work.

Finally, this work strongly suggests the need for further investigations in two directions. First, this work has considered the definitions of REA or REV initially established on homogeneous and isotropic media, but one may wonder if these definitions are still valid or can be refined for strongly anisotropic media made of anisotropic components. Second, our approach has highlighted the crucial role of the anisotropic mechanical properties of the clay matrix. The accurate measurements of these mechanical parameters are still a challenging area of experimental research.

Appendix. The integral range

Here, we borrow definitions and notations from Lantuéjoul (1991). Let us consider (i) a domain of area *S* that is sufficiently large to ensure that the properties of interest may be estimated with good precision (note that the following concepts are defined in 2D but their generalization in 3D is straightforward), and (ii) a stationary random function $(Z(x))_{x\in R^d}$ with mean μ and variance $\sigma^2=D_Z^2$, which are both unknown. In the context of randomness, the average value of Z, named $\bar{Z}$, over the area *S* can be evaluated by the following estimator:

$$Z(S) = \frac{1}{S}\int_S Z(x)dx \qquad (A1)$$

and the variance of this estimator, namely, $D_Z^2(S)$, is given by the following:

$$D_Z^2(S) = \frac{1}{S^2}\int_S \int_S C(y-x)dxdy \qquad (A2)$$

where $C(y-x)$ is the autocovariance function of the *stationary* random function *Z(x)* expressed by the following:

$C(y\text{-}x) = C(h) = E\{[Z(x)\text{-}E(Z)]\,[Z(x+h)\text{-}E(Z)]\}$ (A3)

In other words, the statistical property $D_Z^2(S)$ defined by equation (A2) can be seen as the variance of the average value $\bar{Z}(S)$, which is in fact the effective property to be determined. As explained further, this statistical property $D_Z^2(S)$ is directly linked to the concept of the integral range. The next step requires the definition of the ergodicity assumption, as follows: a random function Z is ergodic if variance $D_Z^2(S)$ tends toward 0 when the size of the domain S becomes infinite, as follows:

$$\lim_{S\to\infty} D_Z^2(S) = 0 \qquad (A4)$$

The concept of the integral range, namely, A_2, is then introduced to define the rate of decrease of this variance at large distances, i.e., in large areas, as follows:

$$A_2 = \lim_{S\to\infty} S\frac{D_Z^2(S)}{D_Z^2} \qquad (A5)$$

This quantity does not always exist. When it does exist, it is nonnegative. If A <+ ∞, for large S, then:

$$D_Z^2(S) \approx \frac{D_Z^2\, A_2}{S} \qquad (A6)$$

Now we return to the problem met in practice. Suppose that the domain S can be decomposed into a union of disjoint subdomains, s_1, …, s_k, all of the same shape and of the same size s. In each subdomain s_i, the average value taken by Z(x) over s_i is as follows:

$$Z(s_i) = \frac{1}{s}\int_{s_i} Z(x)dx \qquad (A7)$$

where s denotes the area of s_i. The "dispersion variance" of the $Z(s_i)$ is now defined as follows:

$$\sigma^2(s|S) = E\left\{\frac{1}{k}\sum_{i=1}^{k}[Z(s_i) - Z(S)]^2\right\} \qquad (A8)$$

or

$$\sigma^2(s|S) = D_Z^2(s) - D_Z^2(S) \qquad (A9)$$

692 Suppose now that the integral range is finite and nonzero and that the area *s* is very large
693 compared to A_2. In this case, the approximation formula (A6) is valid and then equation (A9)
694 can be rewritten as follows:

695 $$\sigma^2(s|S) \approx D_Z^2 A_2 \left(\frac{1}{s} - \frac{1}{S}\right) \quad (A10)$$

696 Now if *S* has been divided into a large number of subdomains, then 1/S can be considered as
697 negligible compared to 1/s and therefore:

698 $$\sigma^2(s|S) \approx \frac{D_Z^2 A_2}{s} \quad (A11)$$

699 Thus, the dispersion variance is inversely proportional to the area of the subdomains, s. From a
700 practical viewpoint, it is this dispersion variance that is calculated to obtain an estimation of A_2
701 by a fitting procedure.

702 **Acknowledgments**. We thank the NEEDS-MIPOR – VARAPE (VARiabilité spatiale des
703 propriétés de l'Argilite au travers d'une approche numérique-expérimentale à Plusieurs
704 Echelles) program for its financial support. A part of this study was also performed in the
705 framework of the research project "ExCiTING" funded by the French National Research
706 Agency (grant agreement ANR-17-CE06-0012). The authors also acknowledge financial
707 support from the European Union (ERDF) and "Région Nouvelle Aquitaine".
708

709 **References**

710 Abou-Chakra Guéry, A., Cormery, F., Shao, J.-F., & Kondo, D. (2010). A comparative
711 micromechanical analysis of the effective properties of a geomaterial: effect of
712 mineralogical compositions. *Computers and Geotechnics*, *37*, 585-593.
713 Andra (2005). Dossier 2005 Argile: Synthesis. Evaluation of the feasibility of a geological
714 pository in an argillaceous formation. Andra, France (available at www.andra.fr).

715 Aplin, A. C., & Larter S. R. (2005). Fluid flow, pore pressure, wettability and leakage in
716 mudstone cap rocks, in: Evaluating Fault and Cap Rock Seals, American Association of
717 Petroleum Geologists Hedberg Series N°2, edited by P. Boult, and J Kaldi, pp 1-12,
718 AAPG, Tulsa, USA.
719 Bennett, R.H., O'Brien, N.R. & Hulbert, M.H. (1991). Determinants of clay and shale
720 microfabric signatures: Processes and mechanisms. In: Bennett, R., Bryant, W., Hulbert,
721 M. (eds), Microstructure of fine grained sediments: from mud to shale, Springer-Verlag,
722 New York, Chapter 2, 5-32.
723 Biot, M. A. (1941). General theory of three-dimensional consolidation. *Journal of Applied*
724 *Physics*, *12*(2), 155-164.
725 Bobko, C., & Ulm, F.J. (2008). The nano-mechanical morphology of shale. *Mechanics of*
726 *Materials, 40*(4), 318-337.
727 Cabrera, J., Beaucaire, C., Bruno, G., De Windt, L., Genty, A., Ramambasoa, N., Rejeb, A.,
728 Savoye, S., & Volant, P. (2001). *Projet Tournemire : Synthèse des Résultats des*
729 *Programmes de Recherche 1995/1999.* IRSN Report.
730 Cariou, S., Dormieux, L., & Skoczylas, F. (2013). An original constitutive law for Callovo-
731 Oxfordian argillite, a two-scale double-porosity material. *Applied. Clay Science*, *80*, 18-
732 30.
733 Christensen, R. M. (2012). *Mechanics of composite materials*. Courier Corporation.
734 Conil, N., Talandier, J., Djizanne, H., de La Vaissière, R., Righini-Waz, C., Auvray, C.,
735 Morlot ; C., & Armand, G. (2018). How rock samples can be representative of in situ
736 condition: A case study of Callovo-Oxfordian claystones., *Journal of Rock Mechanics*
737 *and Geotechnical Engineering*, *10*(4), 613-623.
738 Cosenza, P., Prêt, D., Giraud, A., & Hedan, S. (2015a). Effect of the local clay distribution on
739 the effective elastic properties of shales. *Mechanics of Materials*, *84*, 55-74.

740 Cosenza, P., Prêt, D., & Zamora, M. (2015b). Effect of the local clay distribution on the
741 effective electrical conductivity of clay rocks. *Journal of geophysical research: solid*
742 *earth*, *120(1),* 145-168.
743 Cousin, I., Levitz, P., & Bruand, A. (1996). Three-dimensional analysis of a loamy-clay soil
744 using pore and solid chord distributions. *European Journal of Soil Science*, *47*(4), 439-
745 452.
746 Fauchille, A. L., Hedan, S., Prêt, D., Valle, V., Cabrera, J., & Cosenza, P. (2014). Relationships
747 between desiccation cracking behavior and microstructure of the Tournemire clay rock
748 by coupling DIC and SEM methods. *Proceedings of IS on Geomechanics from Micro*
749 *to Macro, Cambridge, UK. CRC Press/Balkema, Leiden, The Netherlands*, 1421-1424.
750 Fauchille, A.L., (2015). Déterminismes microstructuraux et minéralogiques de la fissuration
751 hydrique dans les argilites de Tournemire : apports couplés de la pétrographie
752 quantitative et de la correlation d'images numériques, PhD thesis of Poitiers University
753 (France) (in French).
754 Fauchille, AL van den Eijnden, A.P., Ma L., Chandler, M., Taylor, K.G., Madi, K., Lee, P.D,
755 Rutter, E. (2018). Variability in spatial distribution of mineral phases in the Lower
756 Bowland Shale, UK, from the mm- to μm-scale: Quantitative characterization and
757 Modeling, *Marine and Petroleum Geology, in press*.
758 Gaboreau, S., Robinet, J. C., & Prêt, D. (2016). Optimization of pore-network characterization
759 of a compacted clay material by TEM and FIB/SEM imaging. *Microporous and*
760 *Mesoporous Materials*, *224*, 116-128.
761 Giraud, A., Huynh, Q. V., Hoxha, D., & Kondo, D. (2007a). Effective poroelastic properties of
762 transversely isotropic rock-like composites with arbitrarily oriented ellipsoidal
763 inclusions. *Mechanics of Materials, 39*(11), 1006-1024.

764 Giraud, A., Huynh, Q. V., Hoxha, D., & Kondo, D. (2007b). Application of results on Eshelby
765 tensor to the determination of effective poroelastic properties of anisotropic rocks-like
766 composites. *International Journal of Solids and Structures, 44*(11), 3756-3772.
767 Hornby, B. E., Schwartz, L. M., & Hudson, J. A. (1994). Anisotropic effective-medium
768 modeling of the elastic properties of shales. *Geophysics*, *59(*10), 1570-1583.
769 Houben, M. E., Desbois, G., & Urai, J. L. (2014). A comparative study of representative 2D
770 microstructures in Shaly and Sandy facies of Opalinus Clay (Mont Terri, Switzerland)
771 inferred form BIB-SEM and MIP methods. *Marine and Petroleum Geology*, *49*, 143-
772 161.
773 Houben, M. E., Barnhoorn, A., Wasch, L., Trabucho-Alexandre, J., Peach, C. J., & Drury, M.
774 R. (2016). Microstructures of early jurassic (Toarcian) shales of Northern
775 Europe. *International Journal of Coal Geology*, *165*, 76-89.
776 Jeulin, D., Kanit, T., & Forest, S. (2004). Representative volume element: a statistical point of
777 view. In *Continuum Models and Discrete Systems* (pp. 21-27). Springer, Dordrecht.
778 Jakobsen, M.J., Hudson, A., Johansen, T.A. (2003). T-matrix approach to shale acoustics,
779 *Geophysical Journal International, 154*, 533-558.
780 Jorand R. 2006, Etude expérimentale de la conductivité thermique: application au forage
781 EST205 du site de Meuse/Haute Marne (Andra), Ph-D Thesis, University of Denis
782 Diderot (Paris) (in French).
783 Kameda, A., Dvorkin, J., Keehm, Y., Nur, A., & Bosl, W. (2006). Permeability-porosity
784 transforms from small sandstone fragments. *Geophysics*, *71*(1), N11-N19.
785 Kanit, T., Forest, S., Galliet, I., Mounoury, V., & Jeulin, D. (2003). Determination of the size
786 of the representative volume element for random composites: statistical and numerical
787 approach. *International Journal of solids and structures*, *40*(13-14), 3647-3679.

788 Kanit, T., N'Guyen, F., Forest, S., Jeulin, D., Reed, M., & Singleton, S. (2006). Apparent and
789 effective physical properties of heterogeneous materials: representativity of samples of
790 two materials from food industry. *Computer Methods in Applied Mechanics and*
791 *Engineering*, *195*(33-36), 3960-3982.
792 Khdir, Y. K., Kanit, T., Zaïri, F., & Nait-Abdelaziz, M. (2013). Computational homogenization
793 of elastic–plastic composites. *International Journal of Solids and Structures*, *50*(18),
794 2829-2835.
795 Keller, L. M., Holzer, L., Schuetz, P., & Gasser, P. (2013). Pore space relevant for gas
796 permeability in Opalinus clay: Statistical analysis of homogeneity, percolation, and
797 representative volume element. *Journal of Geophysical Research: Solid Earth*, *118*(6),
798 2799-2812.
799 Keller, L. M. (2015). On the representative elementary volumes of clay rocks at the
800 mesoscale. *Journal of Geology and Mining Research*, *7*(6), 58-64.
801 Keller, L. M. (2016a). Pore geometry effects on elastic properties of Opalinus
802 Clay. *Geophysics*, *81*(5), D543-D551.
803 Keller, L. M. (2016b). Porosity anisotropy of Opalinus Clay: implications for the poroelastic
804 behaviour. *Geophysical Journal International*, *208*(3), 1443-1448.
805 Klaver, J., Desbois, G., Littke, R., & Urai, J. L. (2015). BIB-SEM characterization of pore space
806 morphology and distribution in postmature to overmature samples from the Haynesville
807 and Bossier Shales. *Marine and petroleum Geology*, *59*, 451-466.
808 Lantuejoul, C. (1991). Ergodicity and integral range. *Journal of Microscopy*, *161*(3), 387-403.
809 Levin, V.M., & Markov, M.G. (2005). Elastic properties of inhomogeneous transversely
810 isotropic rocks. *International Journal of Solids and Structures, 42*(2), 393-408.

Liu, K., & Ostadhassan, M. (2017). Quantification of the microstructures of Bakken shale reservoirs using multi-fractal and lacunarity analysis. *Journal of Natural Gas Science and Engineering*, *39*, 62-71.

Loucks, R. G., Reed, R. M., Ruppel, S. C., & Hammes, U. (2012). Spectrum of pore types and networks in mudrocks and a descriptive classification for matrix-related mudrock pores. *AAPG bulletin*, *96*(6), 1071-1098.

Ma, L., Fauchille, A. L., Dowey, P. J., Pilz, F. F., Courtois, L., Taylor, K. G., & Lee, P. D. (2017). Correlative multi-scale imaging of shales: a review and future perspectives. *Geological Society, London, Special Publications*, *454*, SP454-11.

Markov, M., Levine, V., Mousatov, A., & Kazatchenko, E. (2005). Elastic properties of double-porosity rocks using the differential effective medium model. *Geophysical Prospecting 53*(5), 733-754.

Matheron, G. (1971). The theory of regionalized variables and it applications. *Ecole des Mines de Paris, Paris*.

Mavko, G., Mukerji, T., & Dvorkin, J. (2009). The rock physics handbook: Tools for seismic analysis of porous media. Cambridge University Press.

Niandou, H., Shao, J. F., Henry, J. P., & Fourmaintraux, D. (1997). Laboratory investigation of the mechanical behaviour of Tournemire shale. *International Journal of Rock Mechanics and Mining Sciences*, *34*(1), 3-16.

Ortega, J. A., Ulm, F. J., & Abousleiman, Y. (2007). The effect of the nanogranular nature of shale on their poroelastic behavior. *Acta Geotechnica, 2*(3), 155-182.

Ortega, J. A., Ulm, F. J., & Abousleiman, Y. (2009). The nanogranular acoustic signature of shale. *Geophysics. 74*(3), D65-D84.

834 Pelissou, C., Baccou, J., Monerie, Y., & Perales, F. (2009). Determination of the size of the
835 representative volume element for random quasi-brittle composites. *International*
836 *Journal of Solids and Structures*, *46*(14-15), 2842-2855.
837 Prêt, D. (2003). Nouvelles méthodes quantitatives de cartographie de la minéralogie et de la
838 porosité dans les matériaux argileux : application aux bentonites compactées des
839 barrières ouvragées, p. 257. PhD-Thesis, Poitiers University, France (in French).
840 Prêt, D., Sammartino, S., Beaufort, D., Meunier, A., Fialin, M., Michot, L. (2010a). A new
841 method for quantitative petrography based on image processing of chemical elements
842 maps : Part I. Mineral mapping applied to compacted bentonites. *American*
843 *Mineralogist, 95*, 1379-1388.
844 Prêt, D., Sammartino, S., Beaufort, D., Fialin, M., Sardini, P., Cosenza, P., Meunier, A. (2010b).
845 A new method for quantitative petrography based on image processing of chemical
846 elements maps : Part II. Semi-quantitative porosity maps superimposed on mineral
847 maps. *American Mineralogist, 95*, 1389-1398.
848 Pusch, R., (2006). Clays and nuclear waste management. In: Handbook of Clay Science,
849 Editors: Bergaya, F., Theng, B.K.G., Lagaly, G., Developments in Clay Science,
850 Elsevier, 703-716.
851 Robinet, J. C. Minéralogie, porosité et diffusion dans l'argilite du Callovo-Oxfordien de Bure
852 (Meuse/Haute-Marne, France) de l'échelle centimétrique à micrométrique. PhD thesis,
853 Poitiers University (France) (in French).
854 Robinet, J.C., Prêt, D., Sardini, P., & Coelho, D. (2007). Solute diffusion in Bure argillite at
855 millimeter to micrometer scales: the role of mineral and microstructural heterogenities,
856 3rd. Annual Workshop Proceedings 6th EC FP – FUNMIG IP, Edinburgh 26th-29th
857 November 2007.

858 Robinet, J. C., Sardini, P., Coelho, D., Parneix, J.C., Prêt, D., Sammartino, S., & Altmann, S.
859 (2012). Effects of mineral distribution at mesoscopic scale on solute diffusion in a clay-
860 rich rock: Example of the Callovo-Oxfordian mudstone (Bure, France). *Water*
861 *Resources Research, 48*(5).
862 Rolland du Roscoat, S. R., Decain, M., Thibault, X., Geindreau, C., & Bloch, J. F. (2007).
863 Estimation of microstructural properties from synchrotron X-ray microtomography and
864 determination of the REV in paper materials. *Acta Materialia*, *55*(8), 2841-2850.
865 Song, Y., Davy, C. A., Troadec, D., Blanchenet, A. M., Skoczylas, F., Talandier, J., & Robinet,
866 J. C. (2015). Multi-scale pore structure of COx claystone: Towards the prediction of fluid
867 transport. *Marine and Petroleum Geology*, *65*, 63-82.
868 Torquato, S. (2013). Random heterogeneous materials: microstructure and macroscopic
869 properties (Vol. 16). Springer Science & Business Media.
870 Torquato S., & Stell, G. (1982). Microstructure of two-phase random media. I. The *n*-point
871 probability functions, *Journal of Chemical Physics, 77*, 2071.
872 Ulm, F. J., Delafargue, A., & Constantinides, G. (2005). Experimental microporomechanics. In
873 Applied micromechanics of porous materials (pp. 207-288). Springer Vienna.
874 Withers, P.J. (1989). The determination of the elastic field of an ellipsoidal inclusion in a
875 transversely isotropic medium, and its relevance to composite materials. *Philosophical*
876 *Magazine, A. 59*(4), 759-781.
877 Zhang, D., Zhang, R., Chen, S., & Soll, W. E. (2000). Pore scale study of flow in porous media:
878 Scale dependency, REV, and statistical REV. *Geophysical research letters*, *27*(8),
879 1195-1198.
880 Zhang, W., Zhao, Q., Huang, R., Ma, D., Chen, J., Xu, P., & Que, J. (2017). Determination of
881 Representative Volume Element Considering the Probability that a Sample Can

Represent the Investigated Rock Mass at Baihetan Dam Site, China. *Rock Mechanics and Rock Engineering*, *50*(10), 2817-2825.

887 **Table captions**

888 Table 1. *Geometrical and mineralogical features of both mineral maps used in this work.*

889 Table 2. Input data for the calculations of apparent elastic properties of both shales under study.

890 Table 3. Inverted values of isotropic moduli of the clay phase by the Monte Carle procedure
891 (isotropic model).

892 Table 4. REA estimates obtained from the counting box method.

893 Table 5. Morphological REA size estimates by statistical approach (n=1; error ranging between
894 5 and 10%). The results of inverse regression and integral range are also given.

895 Table 6. Recapitulation of mechanical REA size estimates by statistical approach (n=1; error
896 ranging between 5 and 10%).

897

898 **Figure captions**

899 Figure 1. Microstructure of clay-rocks at various scales (modified from Ulm et al. 2005; Sarout
900 and Guéguen, 2008; Cosenza et al., 2015a).

901 Figure 2. Extraction of the mineral COx map used in this work (modified from Cosenza et al.,
902 2015a).

903 Figure 3. Extraction of the mineral Toar map used in this work (modified from Fauchille, 2015).

904 Figure 4. A. Partitioning of the COx map only used for the counting box method. B. Partitioning
905 of the Toar map used for the counting box method. In both cases, the direction of
906 bedding is indicated.

907 Figure 5 Estimation of the Representative Elementary Area (REA) size of mineral maps by
908 counting box method. Evolution of mean clay fraction with increasing subdomain size
909 (box) and for different starting domains. The coordinates of starting domains are given
910 in the captions boxes (see the origin of the system of Cartesian coordinates in Figures 2
911 and 3).

912 a. COx map. The x-coordinates of the starting domains is 250 µm. The horizontal dashed
913 lines indicate the range of mean clay fraction corresponding to $(1 \pm \varepsilon)\overline{\phi}_{COx}$ with
914 $\overline{\phi}_{COx}$=0.504 (50.4%) and ε=0.1(10%)

915 b. Toar map. The horizontal dashed lines indicate the range [62.9-76.9%] corresponding
916 to $(1 \pm \varepsilon)\overline{\phi}_{Toar}$ with $\overline{\phi}_{Toar}$=0.699 (69.9%) and ε=0.1(10%).

917 Figure 6. Evolution of the mean clay fraction and related standard deviation *versus* the
918 subdomain size for both maps.

Figure 7. Determination of the "morphological" integral range A_2. Evolution of the pseudovariance of the clay fraction, i.e., Variance ($\bar{\varphi}_{arg}(1\text{-}\bar{\varphi}_{arg})$) as a function of 1/S, where S is the box size area. A linear fit is indicated by a bold line. a. COx map. b. Toar map.

Figure 8. REA size, L_{REA} (µm), as a function of error (%) for one realization (n=1) for both mineral maps.

Figure 9. Mean value and dispersion (standard deviation) of the apparent elastic moduli as a function of the subdomain size L in the case of the anisotropic model and isotropic model. a: COx map. b: Toar map.

Figure 10. Determination of the "mechanical" integral range A_2. Evolution of the variance of the elastic modulus of the anisotropic and isotropic models as a function of the subdomain area. Power fits are also indicated to calculate the integral range values. a. COx map. b. Toar map.

Figure 11. Mechanical REA size, L_{REA} (µm), as a function of error (%) for one realization (n=1). Both elastic moduli, i.e., the bulk modulus and shear modulus; both micromechanical models, i.e., the anisotropic model and isotropic model, are considered. a. COx map. b. Toar map.

Figure 12. Zoom of the evolutions of the pseudo-variance of clay fraction i.e., Variance($\bar{\varphi}_{arg}(1\text{-}\bar{\varphi}_{arg})$) as a function of subdomain area of both maps. R^2 values of both fits are also given.

940

941 Table 1. *Geometrical and mineralogical features of both mineral maps used in this work.*

Map	Resolution (µm)	Total number of pixels	Dimensions (pixels)	Dimensions (µm)	Clay minerals (%)	Quartz (%)	Calcite (%)
COx	2	384 000	250 x 1536	500 x 3072	50.4	13.8	25.0
Toar	0.625	16 10^6	4000 x 4000	2500 x 2500	69.9	13.2	14.1

942

943

944

945 Table 2. Input data for the calculations of apparent elastic properties of both shales under study.

Shale	Macroscopic (reference) shale elastic modulus (GPa)	Non-clay phase Isotropic elastic modulus Weighted average (GPa)[b]	Clay phase Transverse isotropic (undrained) modulus (GPa)[c]
Callovo-Oxfordian claystone	Bulk modulus[a] 11.5 Shear modulus[a] 5.3	Bulk modulus 56.3 Shear modulus 38.5	C_{11}= 14.3 C_{12}=4.6 C_{13}=2.7 C_{33}=8.9 C_{44}=2.8
Tournemire argillite	Bulk modulus[d] 9.2 Shear modulus[d] 6.5	Bulk modulus 53.9 Shear modulus 37.5	C_{11}= 14.3 C_{12}=4.6 C_{13}=2.7 C_{33}=8.9 C_{44}=2.8

946 [a]ANDRA (2009) (undrained Poisson ratio: v^u=0.3)

947 [b]Table 1 and Mavko et al. (2009)

948 [c]Ulm et al. (2005); Cosenza et al. (2015b)

949 [d]Niandou et al. (1997)

950

951 Table 3. Inverted values of isotropic moduli of clay phase by Monte Carle procedure (isotropic
952 model).

Shale	Clay phase Inverted isotropic modulus (GPa)	Relative difference between reference value and calculated value from inverted clay phase moduli (%)
Callovo-Oxfordian claystone	Bulk modulus 5.0 Shear modulus 1.6	Bulk modulus 0.3 Shear modulus 1.4
Tournemire argillite	Bulk modulus 5.3 Shear modulus 3.7	Bulk modulus 1.6 Shear modulus 0.1

953

954

955 Table 4. REA estimates obtained by counting box method.

956

Map	Area (Ai)	Center of area (Ci)	Asymptotic value (φ_∞) (%)	REA estimate (L_{REA}) (µm) ε=0.1 (10%)	REA estimate (L_{REA}) (µm) ε=0.05 (5%)
COx	A1	C1 (x=250µm, z=250µm)	49.0	262	314
	A2	C2 (x=250µm, z=750µm)	48.6	322	438
	A3	C3 (x=250µm, z=1250µm)	49.4	128	170
	A4	C4 (x=250µm, z=1750µm)	51.6	72	86
	A5	C5 (x=250µm, z=2250µm)	52.4	202	310
	A6	C6 (x=250µm, z=2500µm)	51.5	50	86
			Mean: 51.5	Mean: 172.7	Mean: 234.0
			St. Dev.: 1.6	St. Dev.: 108.0	St. Dev.: 142.6
Toar	A1	C1 (x=625µm, z=625µm)	71.4	163	179
	A2	C2 (x=1250µm, z=625µm)	68.5	71	749
	A3	C3 (x=625µm, z=1250µm)	70.2	214	260
	A4	C4 (x=1250µm, z=1250µm)	69.1	68	576
			Mean: 69.8	Mean: 129.0	Mean: 441.0
			St. Dev.: 1.3	St. Dev.: 71.8	St. Dev.: 267.4

957

Table 5. Morphological REA size estimates by statistical approach (n=1; error ranging between 5 and 10%). The results of inverse regression and integral range are also given.

Shale	Statistical morphological REA		
	Regression $\frac{D_\varphi^2(S)}{\bar{\varphi}(1-\bar{\varphi})} = \frac{A_2}{S}$	Integral range A_2	REA size estimates (µm) ($\varepsilon \in [5,10]\%$)
Callovo-Oxfordian claystone	$\frac{D_\varphi^2(S)}{\bar{\varphi}(1-\bar{\varphi})} = \frac{106.6}{S}$ $R^2 = 0.96$	106.6	205-410
Tournemire argillite	$\frac{D_\varphi^2(S)}{\bar{\varphi}(1-\bar{\varphi})} = \frac{703}{S}$ $R^2 = 0.36$	703	345-696

Table 6. Recapitulation of mechanical REA size estimates by statistical approach (n=1; error ranging between 5 and 10%).

Shale	Statistical mechanical REA							
	Anisotropic model				Isotropic model			
	Bulk modulus		Shear modulus		Bulk modulus		Shear modulus	
	Integral range A_2	REA size estimates (µm) $\varepsilon \in [5,10]\%$	Integral range A_2	REA size estimates (µm) $\varepsilon \in [5,10]\%$	Integral range A_2	REA size estimates (µm) $\varepsilon \in [5,10]\%$	Integral range A_2	REA size estimates (µm) $\varepsilon \in [5,10]\%$
Callovo-Oxfordian claystone	27.5	353-765	27.7	574-1251	28.2	253-512	29.4	338-664
Tournemire argillite	37.4	743-1759	37.9	748-1772	38.4	687-1594	38.3	720-1688

963 Figure 1. Microstructure of clay-rocks at various scales (modified from Ulm et al. 2005; Sarout
964 and Guéguen, 2008; Cosenza et al., 2015a).

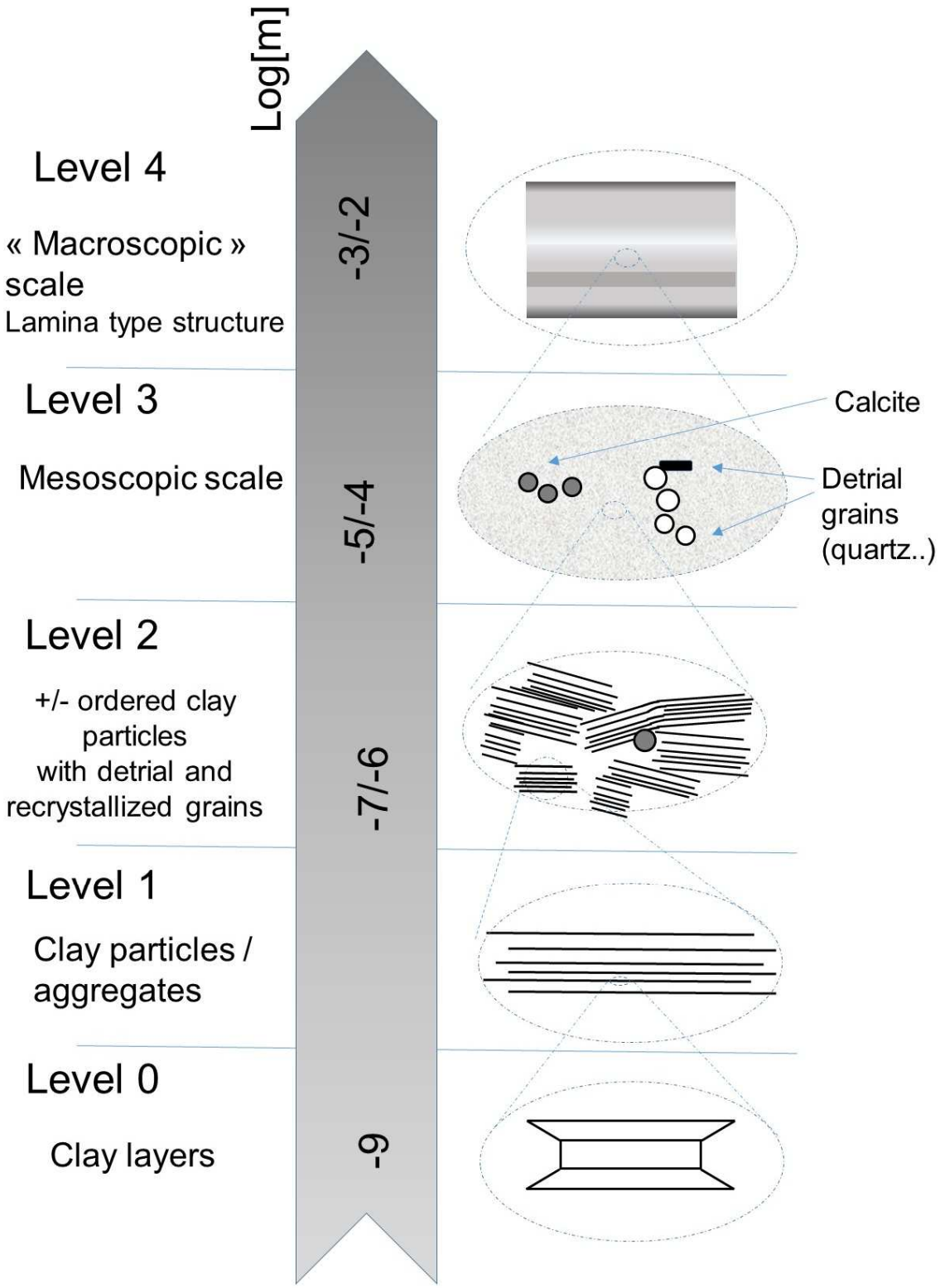

965
966
967

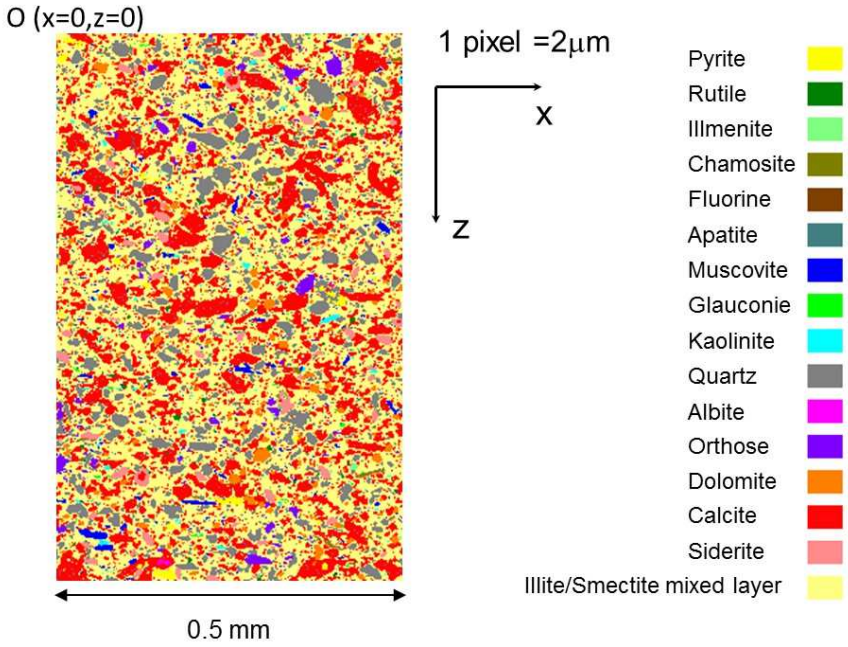

Figure 2. Extraction of the mineral COx map used in this work (modified from Jorand, 2006).

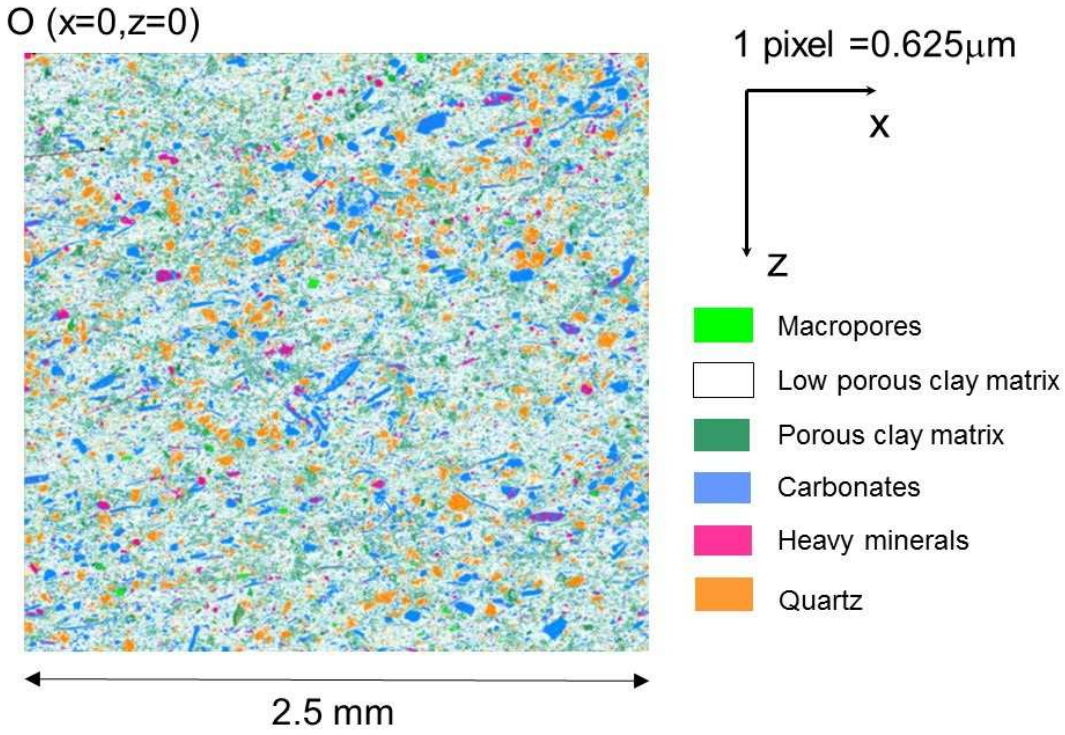

Figure 3. The mineral Toar map used in this work (modified from Fauchille, 2015).

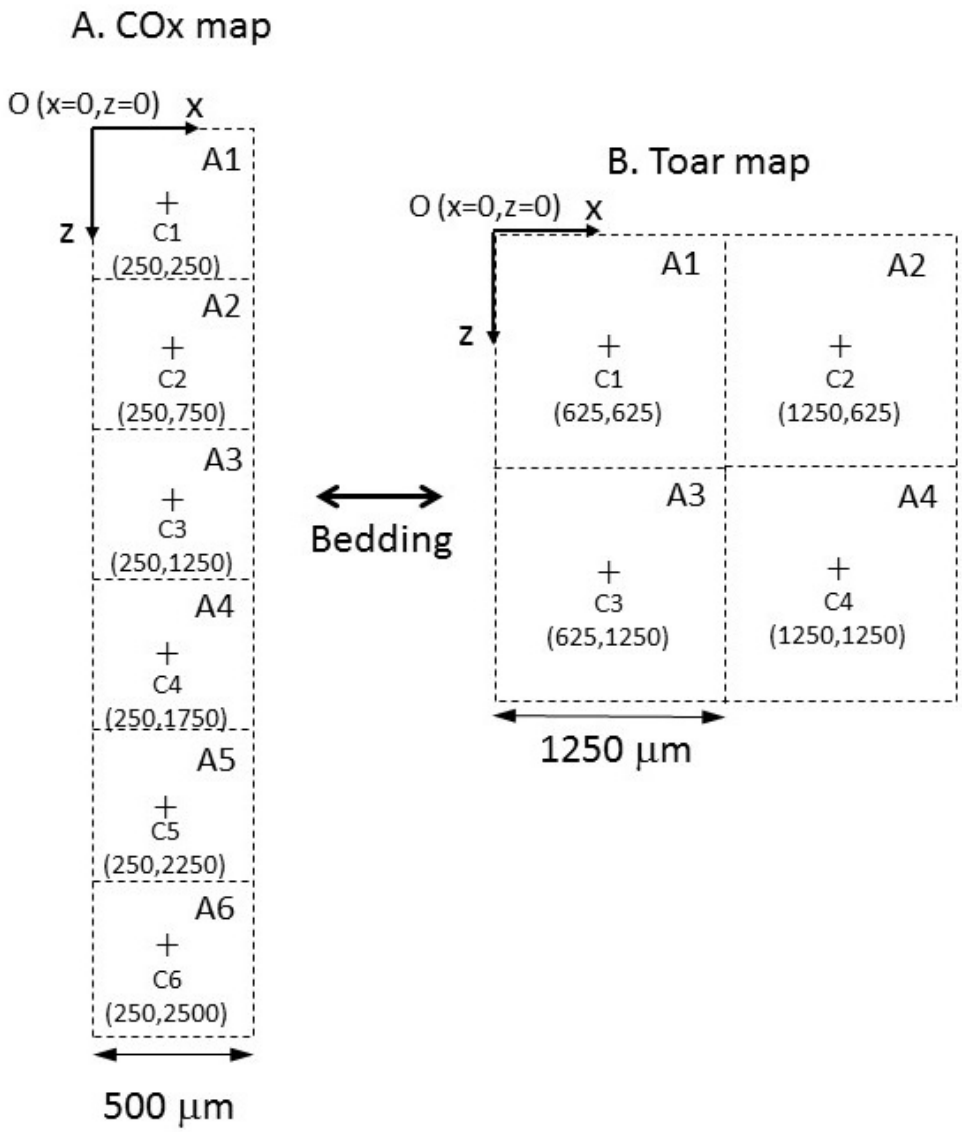

Figure 4. A. Partitioning of the COx map only used for counting box method. B. Partitioning of the Toar map used for counting box method. In both cases, the direction of bedding is indicated.

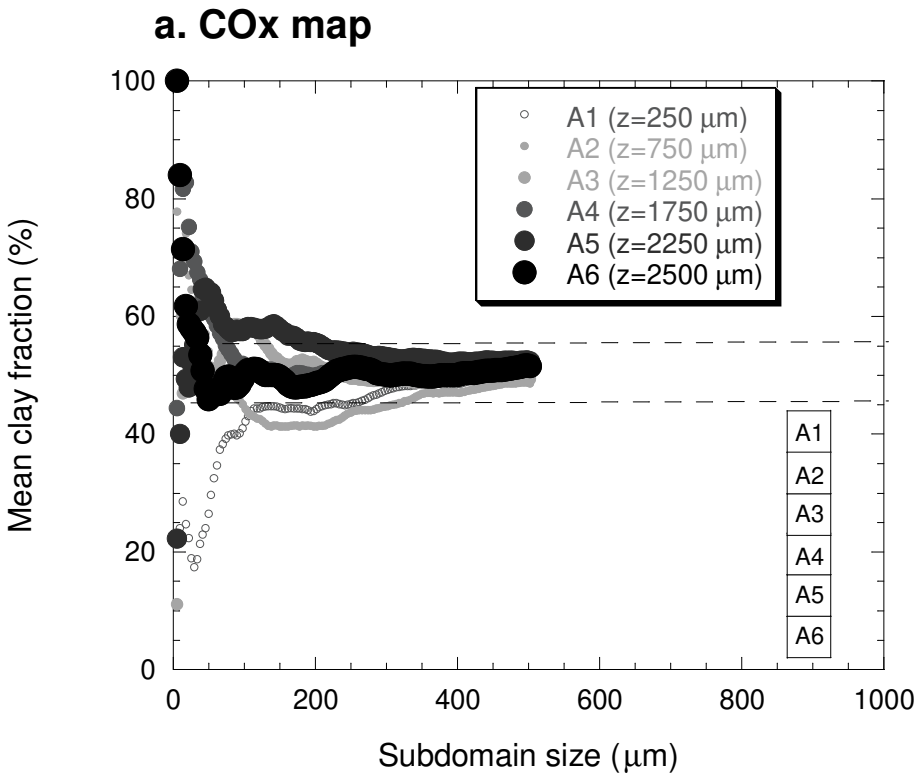

982

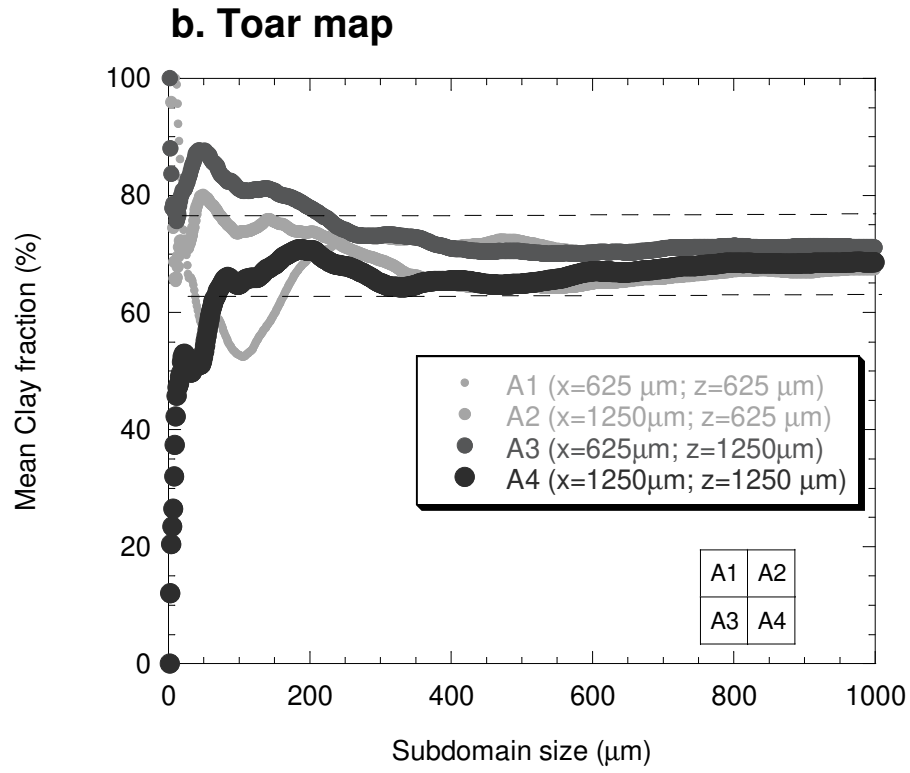

983

984 Figure 5. Estimation of the Representative Elementary Area (REA) size of mineral maps by
985 counting box method. Evolution of mean clay fraction with increasing subdomain size
986 (box) and for different starting domains. The coordinates of starting domains are given
987 in the captions boxes (see the origin of the system of Cartesian coordinates in Figures 2
988 and 3).

a. COx map. The x-coordinates of the starting domains is 250 μm. The horizontal dashed lines indicate the range of mean clay fraction corresponding to $(1 \pm \varepsilon)\overline{\phi}_{COx}$ with $\overline{\phi}_{COx}$=0.504 (50.4%) and ε=0.1(10%).

b. Toar map. The horizontal dashed lines indicate the range [62.9-76.9%] corresponding to $(1 \pm \varepsilon)\overline{\phi}_{Toar}$ with $\overline{\phi}_{Toar}$=0.699 (69.9%) and ε=0.1(10%).

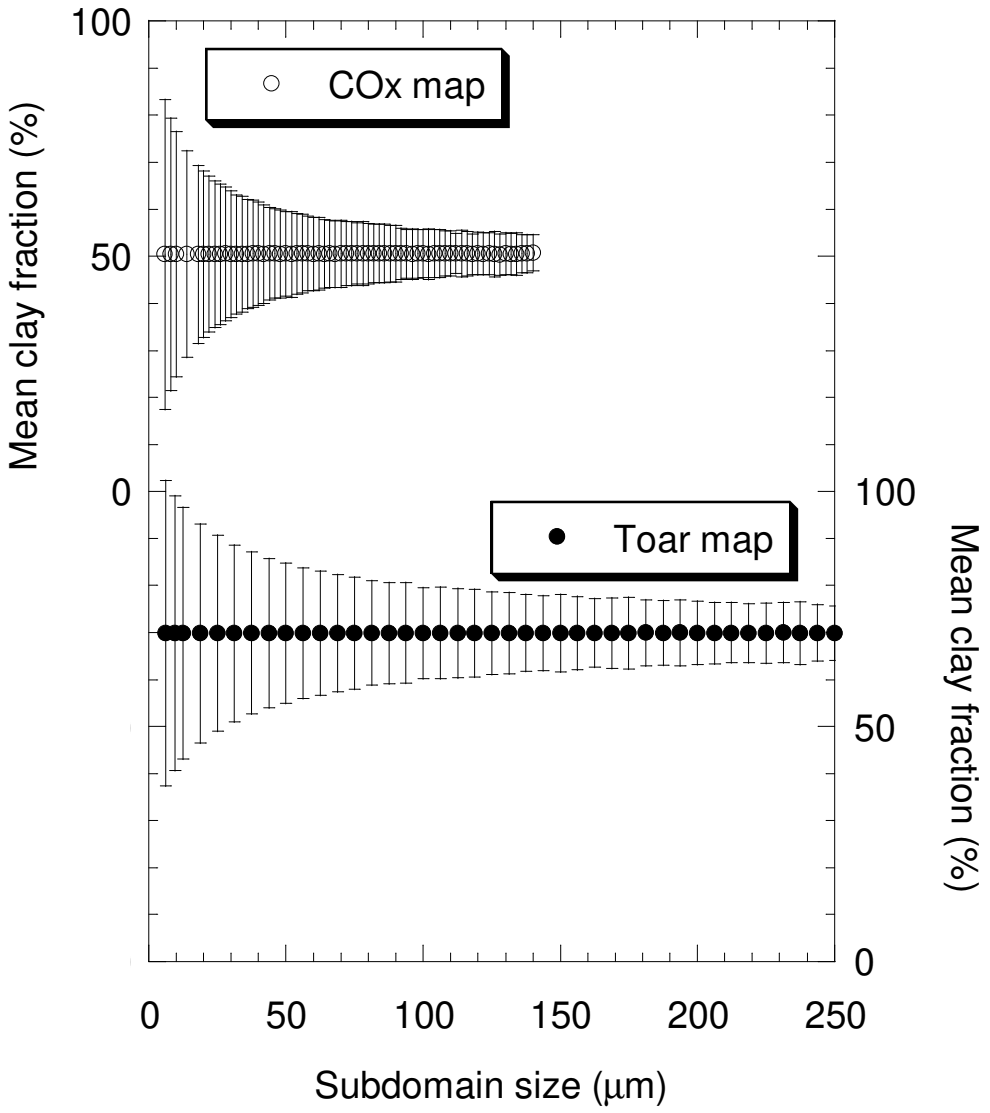

996

997 Figure 6. Evolution of the mean clay fraction and related standard deviation versus the
998 subdomain size *L* for both maps.

999

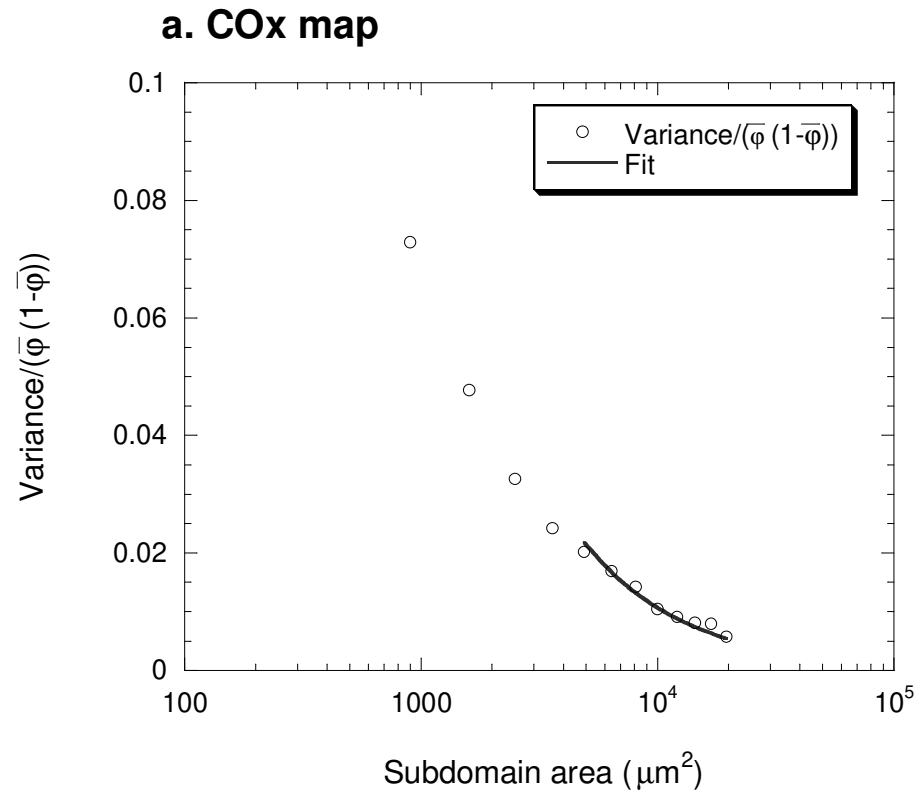

1000

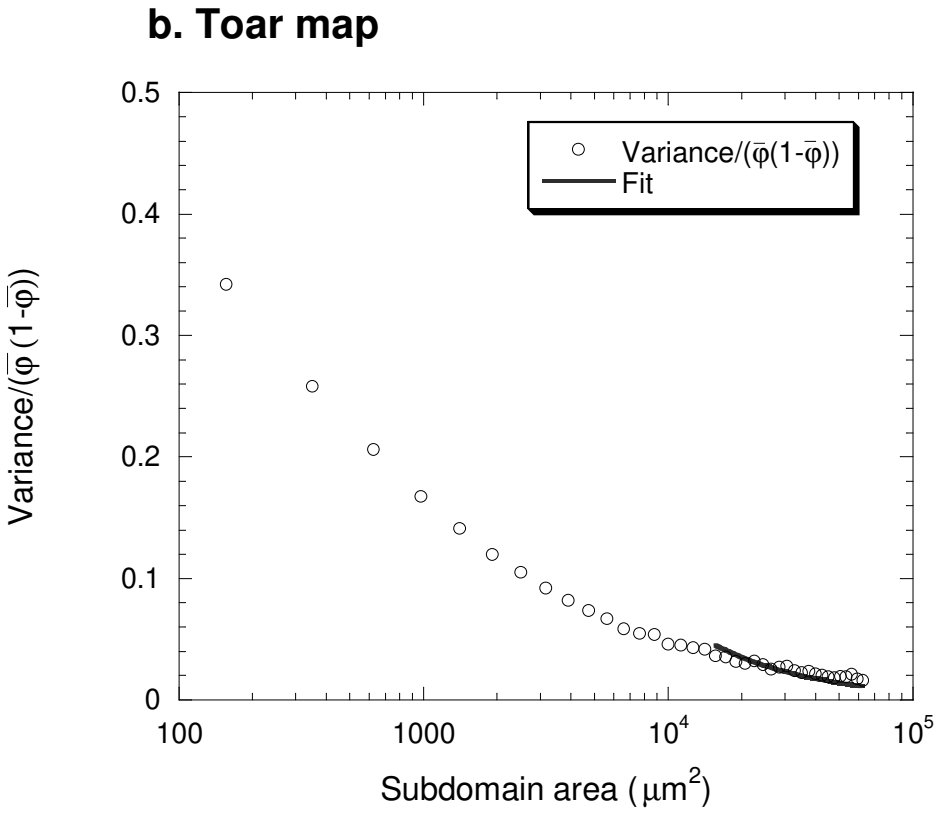

1001

1002 Figure 7. Determination of the "morphological" integral range A_2. Evolution of the pseudovariance of
1003 the clay fraction, i.e., Variance ($\bar{\varphi}_{arg}(1\text{-}\bar{\varphi}_{arg})$) as a function of 1/S, where S is the box size area.
1004 A linear fit is indicated by a bold line. a. COx map. b. Toar map.

1005

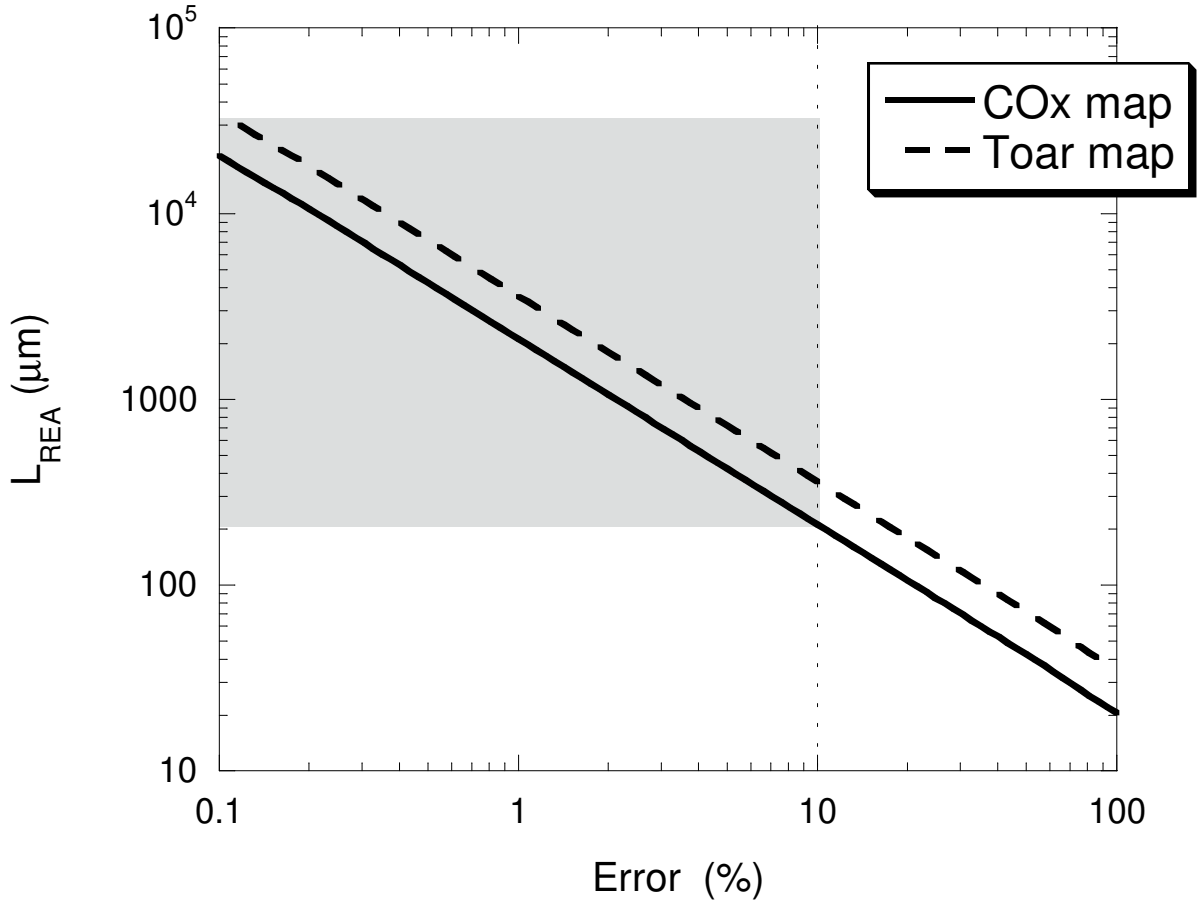

Figure 8. Morphological REA size, L_{REA} (µm) as a function of error (%) for one realization (n=1) for both mineral maps.

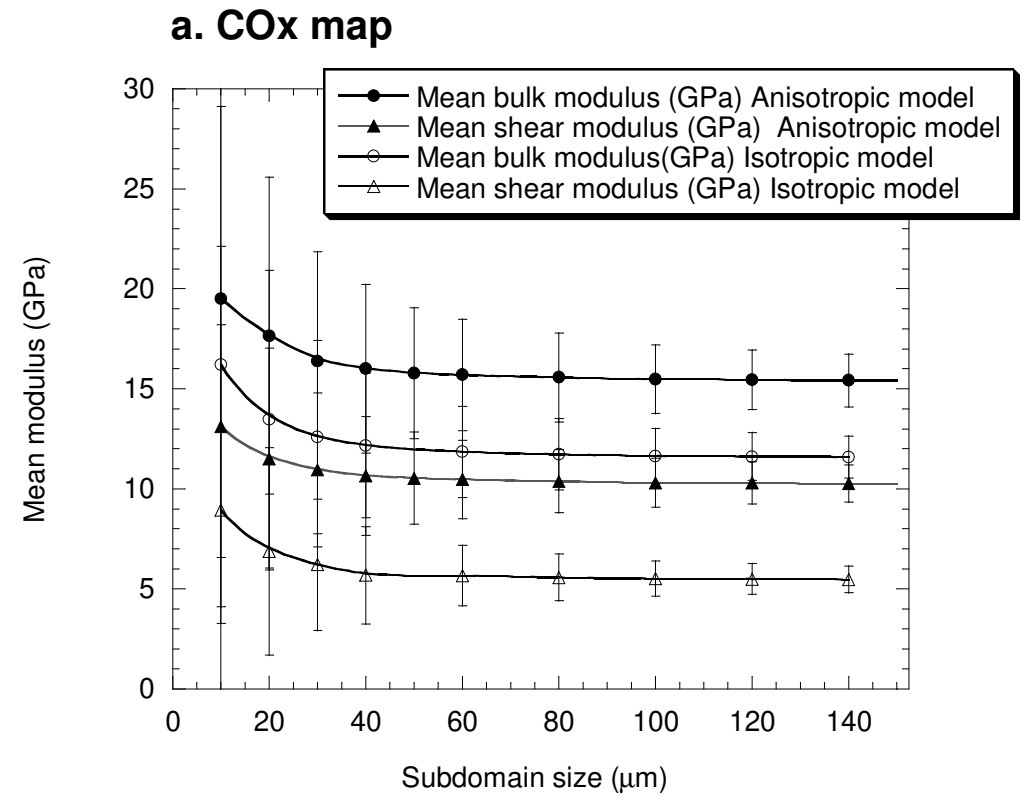

1010

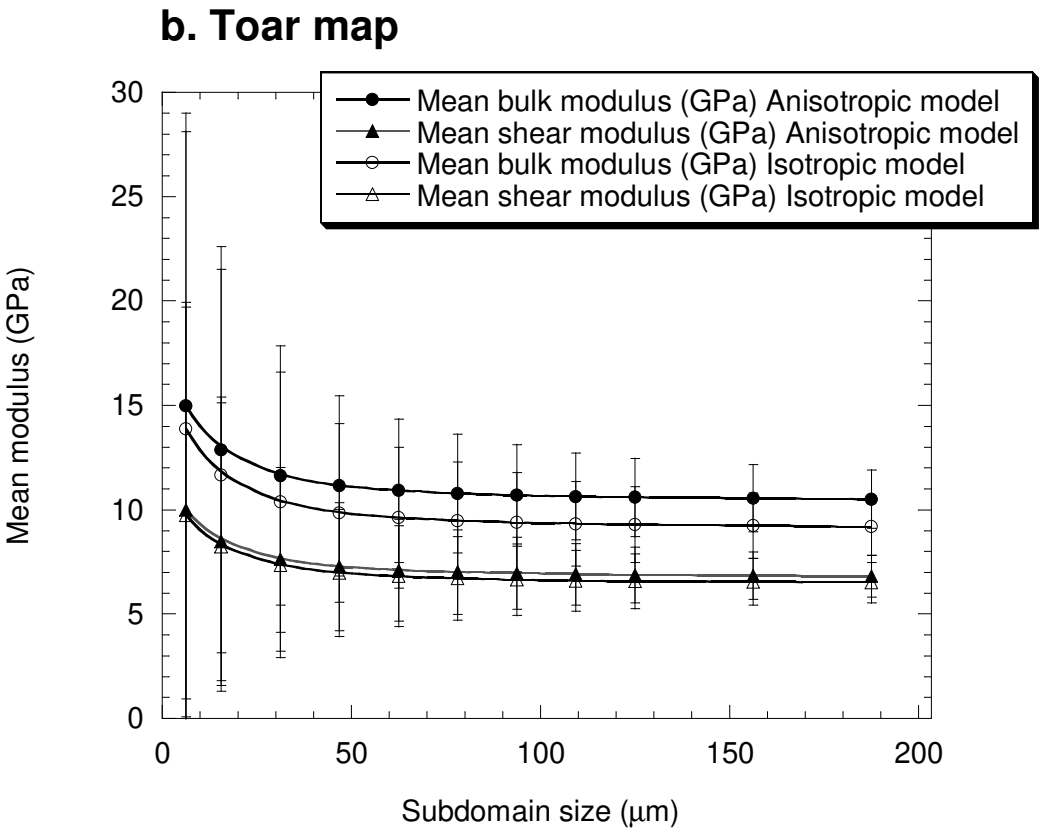

1011

1012 Figure 9. Mean value and dispersion (standard deviation) of the apparent elastic moduli as a
1013 function of the subdomain size L in the case of the anisotropic model and isotropic
1014 model. a: COx map. b: Toar map.

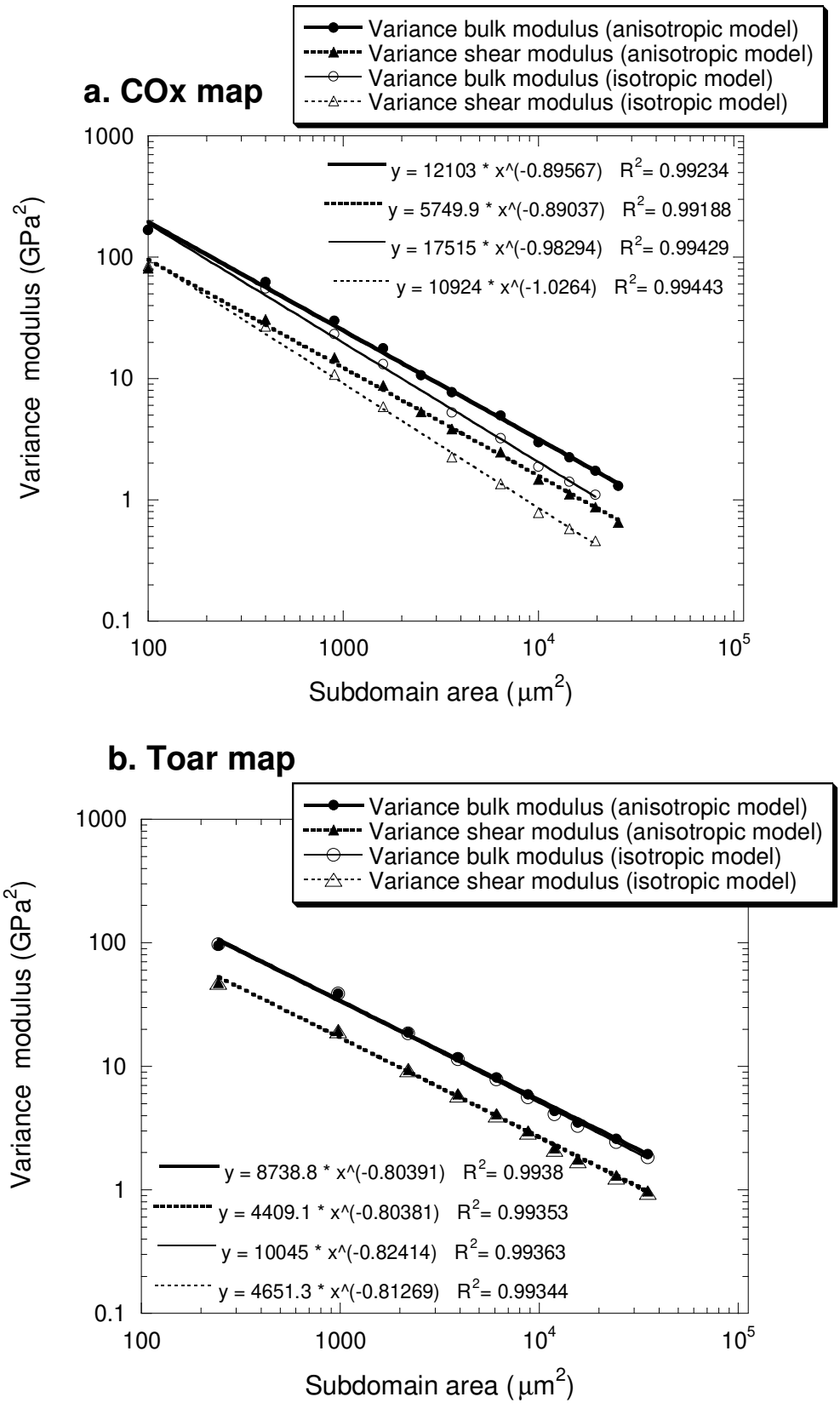

Figure 10. Determination of the "mechanical" integral range A_2. Evolution of the variance of the elastic modulus of the anisotropic and isotropic models as a function of the subdomain area. Power fits are also indicated to calculate the integral range values. a. COx map. b. Toar map.

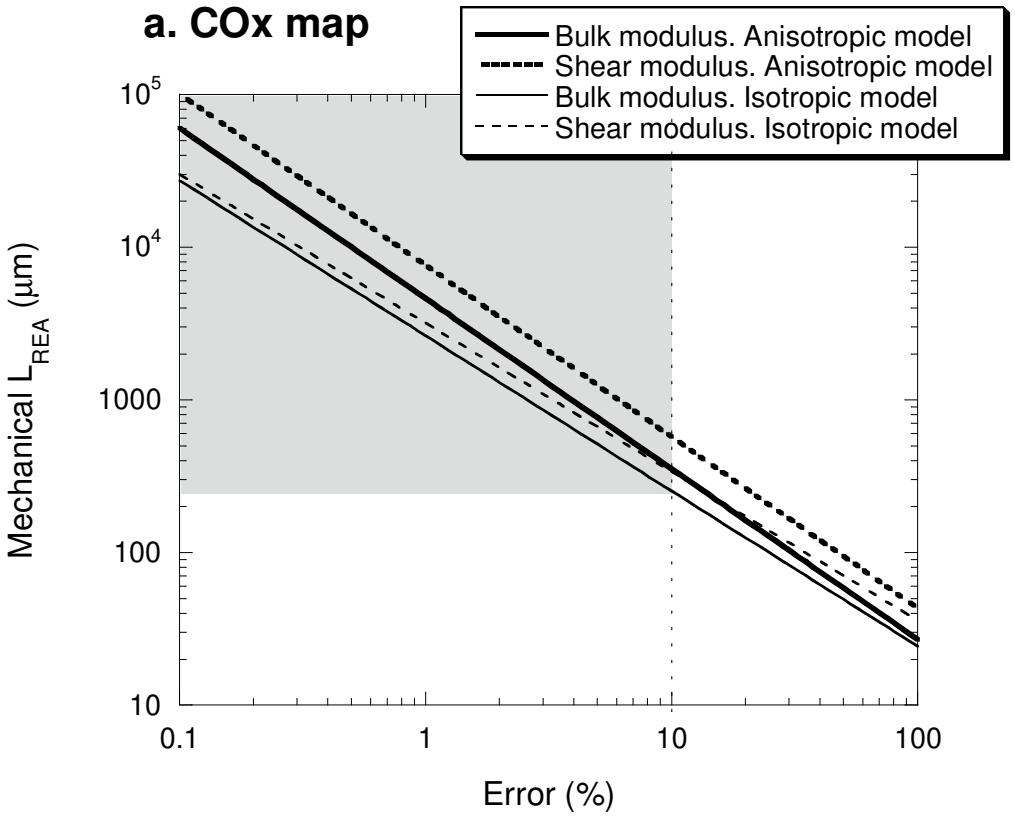

1021

1022

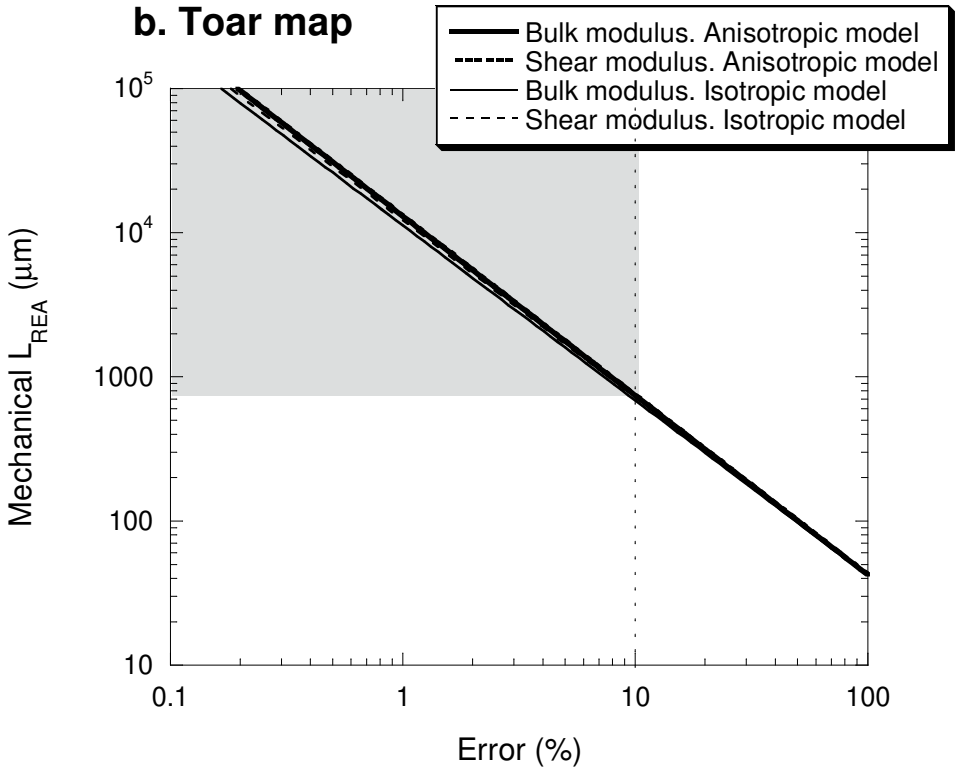

1023

1024 Figure 11. Mechanical REA size, L_{REA} (μm), as a function of error (%) for one realization (n=1). Both
1025 elastic moduli, i.e., the bulk modulus and shear modulus; both micromechanical models, i.e.,
1026 the anisotropic model and isotropic model, are considered. a. COx map. b. Toar map.

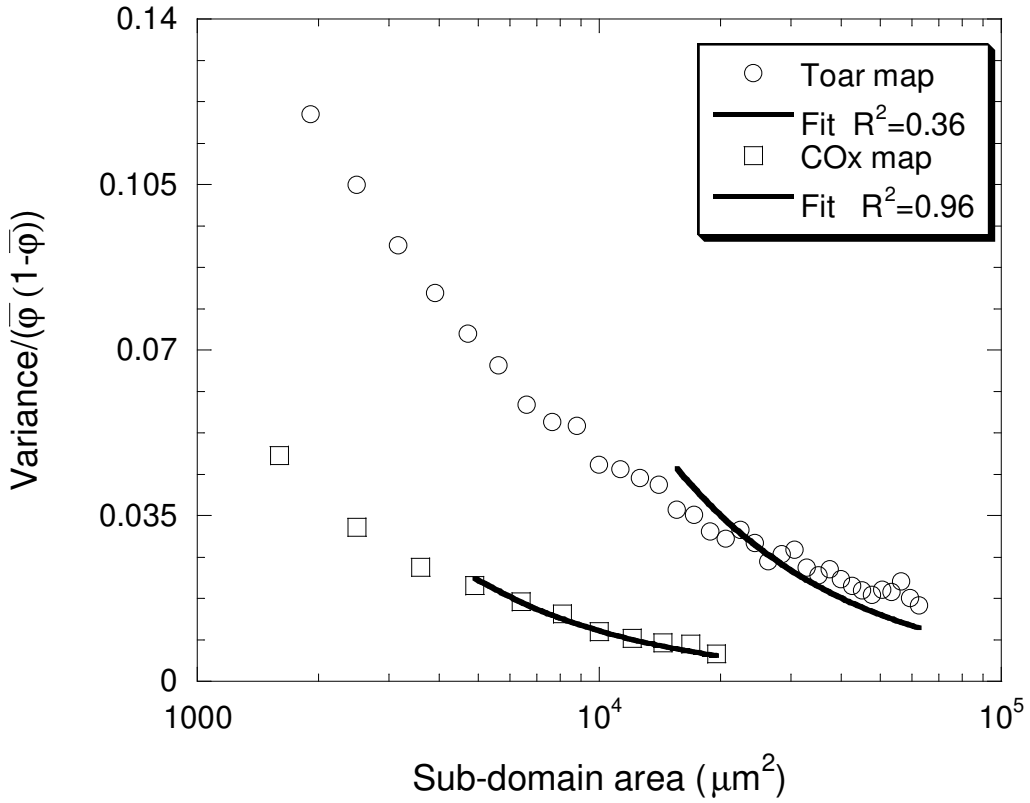

Figure 12. Zoom of the evolutions of the pseudo-variance of clay fraction i.e., Variance($\bar{\varphi}_{arg}$(1-$\bar{\varphi}_{arg}$)) as a function of subdomain area of both maps. R^2 values of both fits are also given.